

## Injection of Tibetan crust beneath the south Qaidam Basin: Evidence from INDEPTH IV wide-angle seismic data

M. S. Karplus,<sup>1</sup> W. Zhao,<sup>2</sup> S. L. Klemperer,<sup>1</sup> Z. Wu,<sup>2</sup> J. Mechie,<sup>3</sup> D. Shi,<sup>2</sup> L. D. Brown,<sup>4</sup> and C. Chen<sup>4</sup>

Received 4 August 2010; revised 19 March 2011; accepted 3 April 2011; published 7 July 2011.

[1] The International Deep Profiling of Tibet and the Himalaya Phase IV (INDEPTH IV) active source seismic profile in northeast Tibet extends 270 km roughly north-south across the Songpan-Ganzi terrane, the predominantly strike-slip North Kunlun Fault (along the Kunlun suture), the East Kunlun Mountains, and the south Qaidam Basin. Refraction, reflection, and gravity modeling provide constraints on the velocity and density structure down to the Moho. The central Qaidam Basin resembles average continental crust, whereas the Songpan-Ganzi terrane and East Kunlun Mountains exhibit thickened, lower-velocity crust also characteristic of southern Tibet. The crustal thickness changes from 70 km beneath the Songpan-Ganzi terrane and East Kunlun Mountains to 50 km beneath the Qaidam Basin. This jump in crustal thickness is located ~100 km north of the North Kunlun Fault and ~45 km north of the southern Kunlun-Qaidam boundary, farther north than previously suggested, ruling out a Moho step caused by a crustal-penetrating North Kunlun Fault. The Qaidam Moho is underlain by crustal velocity material (6.8–7.1 km/s) for ~45 km near the crustal thickness transition. The southernmost 10 km of the Qaidam Moho are underlain by a 70 km reflector that continues to the south as the Tibetan Moho. The apparently overlapping crustal material may represent Songpan-Ganzi lower crust underthrusting or flowing northward beneath the Qaidam Basin Moho. Thus the high Tibetan Plateau may be thickening northward into south Qaidam as its weak, thickened lower crust is injected beneath stronger Qaidam crust.

**Citation:** Karplus, M. S., W. Zhao, S. L. Klemperer, Z. Wu, J. Mechie, D. Shi, L. D. Brown, and C. Chen (2011), Injection of Tibetan crust beneath the south Qaidam Basin: Evidence from INDEPTH IV wide-angle seismic data, *J. Geophys. Res.*, *116*, B07301, doi:10.1029/2010JB007911.

### 1. Introduction

[2] The initial collision of the Indian subcontinent into the Eurasian plate between 53 and 58 Ma [Guillot *et al.*, 2003; Leech *et al.*, 2005] and subsequent compression thickened and uplifted the lithosphere to form the Himalaya and the Tibetan Plateau [Yin and Harrison, 2000; Yin, 2006]. The modern Tibetan Plateau is a complex amalgamation of terranes accreted during the closure of the Qilian and Tethys oceans [Yin and Harrison, 2000] (Figure 1).

[3] The evolution of the orogen and the continued growth of the Tibetan Plateau are active areas of research. Seismic images show the Indian lithosphere subducting beneath Tibet

from the south [Zhao *et al.*, 1993; Kosarev *et al.*, 1999] and underplating the Himalayas and Tibet [Nábelek *et al.*, 2009] as well as, perhaps, the Eurasian plate dipping beneath the plateau from the north [Kind *et al.*, 2002, Zhao *et al.*, 2010]. Hypotheses for accommodation of compression include (1) the lithosphere deforms continuously as a thin viscous sheet [England and Houseman, 1986], (2) material escapes laterally along the east trending strike-slip faults that developed along comparatively weak areas of crust at the suture zones [e.g., Tapponnier and Molnar, 1976; Tapponnier *et al.*, 2001], and (3) material escapes laterally via channel flow in the middle to lower crust [e.g., Zhao and Morgan, 1987; Clark and Royden, 2000; Beaumont *et al.*, 2004].

[4] In this study, we analyze a new wide-angle reflection and refraction profile collected across the NE Tibetan Plateau as part of the project International Deep Profiling of Tibet and the Himalaya, phase IV (INDEPTH IV). The INDEPTH project has studied the lithospheric structure and composition of Tibet since 1992 [e.g., Zhao *et al.*, 1993], progressively building a geophysical and geological transect across the entire plateau from south to north and culminating in INDEPTH IV. The INDEPTH IV profile crosses the Songpan-Ganzi terrane (SG), South Kunlun Fault (SKF), North Kunlun

<sup>1</sup>Department of Geophysics, Stanford University, Stanford, California, USA.

<sup>2</sup>Chinese Academy of Geological Sciences, Beijing, China.

<sup>3</sup>Geophysical Deep Sounding Section, Deutsches GeoForschungsZentrum, Potsdam, Germany.

<sup>4</sup>Department of Earth and Atmospheric Sciences, Cornell University, Ithaca, New York, USA.

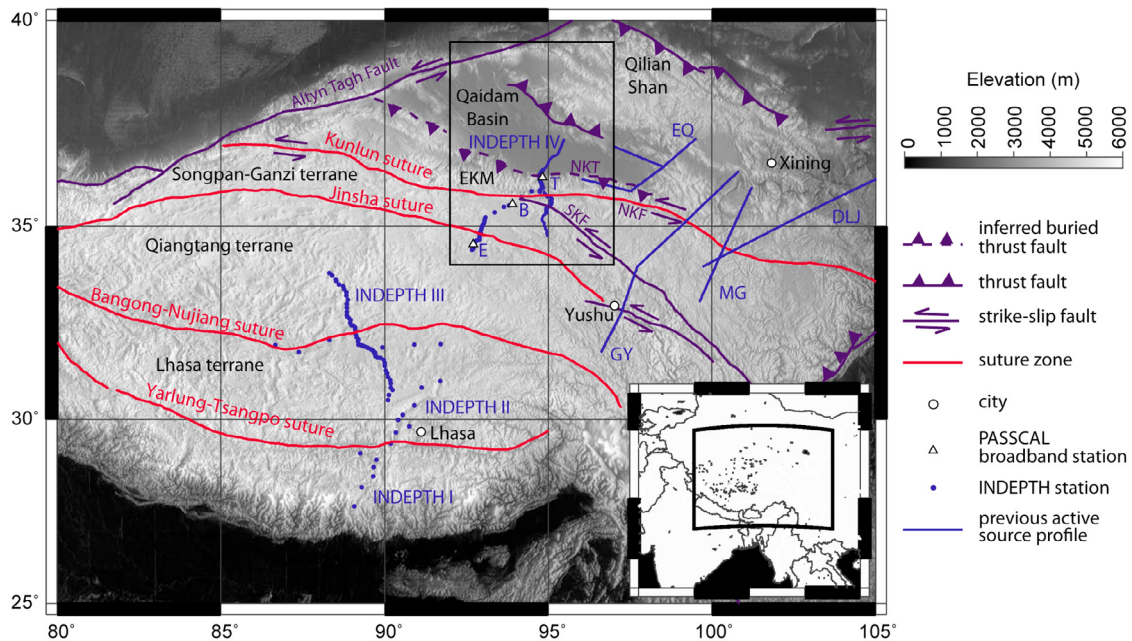


**Figure 1.** Tectonic and topographic map of Tibet. Previous active source seismic profiles include: east Qaidam profile (EQ), Gonghe-Yushu profile (GY) [Galvé *et al.*, 2002], Darlag-Lanzhou-Jingbian profile (DLJ) [Liu *et al.*, 2006], and Moba-Guide profile (MG) [Zhang *et al.*, 2011]. Program for Array Seismic Studies of the Continental Lithosphere (PASSCAL) broadband stations (1991–1992 deployment) are ERDO, BUDO, and TUNL (E, B, and T) [Vergne *et al.*, 2002]. SKF, South Kunlun Fault; NKF, North Kunlun Fault; NKT, North Kunlun Thrust; EKM, East Kunlun Mountains. The black box surrounds the INDEPTH IV profile area displayed in Figure 3. Inset map shows the broader regional setting.

Fault (NKF), East Kunlun Mountains (EKM), and south-to-central Qaidam Basin (QB) near the city of Golmud (Figure 1). The SKF is a thrust fault in the Bayanhar thrust belt within the SG. The Mesozoic Kunlun suture is the boundary across which the Songpan-Ganzi and Kunlun-Qaidam terranes collided, and the active, left-lateral strike-slip NKF roughly follows the location of that suture. The boundary between the East Kunlun Mountains and the Qaidam Basin (Kunlun-Qaidam border or KQB) is the topographic front between the high central Tibetan plateau (average elevation over 4500 m) and the largest basin within the plateau, the QB (average elevation about 2800 m).

[5] Here we present new shallow and deep crustal  $P$  wave velocity models across NE Tibet derived from traveltimes modeling of explosive sources and two local earthquakes recorded by our high-density receiver spreads. Six intracrustal reflections,  $PmP$  (Moho reflection), and  $Pn$  (sub-Moho refraction) constrain crustal structure and thickness along the profile. We compare our new velocity models to previously proposed crustal-scale tectonic models. Our data are inconsistent with a simple, crustal-penetrating NKF or Kunlun suture juxtaposing thicker Tibetan Plateau crust against thinner Qaidam Basin crust [e.g., Chung *et al.*, 2005; Li *et al.*, 2011] or a south directed subduction of the QB offsetting the Moho [Yin *et al.*, 2008b]. At depths below 100 km, the possibility of south vergent subduction of Asian crust [Kind *et al.*, 2002; Zhao *et al.*, 2010] is not addressed by our data. We present a new crustal injection model, based

on our velocity and density modeling, with Tibetan lower-crustal material outflowing or extruding from the East Kunlun Mountains beneath the Qaidam Basin.

## 2. Geotectonic Setting

[6] The INDEPTH IV profile traverses two of Tibet's main crustal blocks or geologic terranes, the SG and the Kunlun-Qaidam (KQ) (Figure 1) [e.g., Sengör *et al.*, 1988], separated by the Anyimaqen-Kunlun-Muztagh suture (Kunlun suture). Many details of the geotectonic history of northeast Tibet remain unknown or contentious. Geochronologic and mapping studies suggest the Kunlun suture was an active subduction zone from 250 to 200 Ma [Roger *et al.*, 2003] until the closure of the Songpan-Ganzi Ocean (Figure 2), which brought the SG and KQ terranes together.

[7] Published terminology for the faults in the northern Tibetan Plateau is confusing, so our terminology (SKF, South Kunlun Fault; NKF, North Kunlun Fault; NKT, North Kunlun Thrust; see Figure 3) is adopted from a widely cited review [Yin and Harrison, 2000] and a recent Chinese publication in the international literature [Shi *et al.*, 2009]. Our SKF and NKF [Shi *et al.*, 2009] are the Kusaihu and Xidatan active faults of Wu *et al.* [2009]. Our NKF is the generic “Kunlun Fault” of many papers [e.g., Zhu and Helmberger, 1998; Yin and Harrison, 2000]. Our NKT [Song and Wang, 1993; Chen *et al.*, 1999; Yin and Harrison, 2000] is also known as the Qaidam Border Fault [Zhu and Helmberger, 1998; Klemperer, 2006] and the South Qaidam Fault [Clark

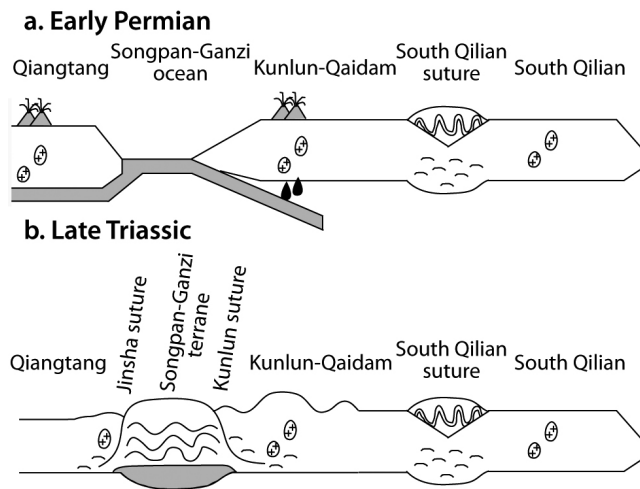


**Figure 2.** Cross sections showing the geologic evolution of northeast Tibet during (a) early Permian after the formation of the south Qilian suture, with deep marine deposition occurring in the Songpan-Ganzi ocean along with arc volcanism beneath the southern Kunlun-Qaidam terrane and volcanism beneath the Qiangtang terrane, and during (b) the Late Triassic after closure of the Songpan-Ganzi ocean. Gray areas represent oceanic crust. Adapted from *Yin and Harrison* [2000].

*et al.*, 2010]. Note that the NKT is certainly a blind thrust system where the INDEPTH IV profile crosses it [Bally *et al.*, 1986], leading *Yin et al.* [2007] to doubt its existence as the north vergent feature shown in our Figure 3.

### 2.1. Songpan-Ganzi Terrane

[8] The SG terrane features at least several kilometers thickness of Triassic deep marine deposits known as the Bayan Har or the Songpan-Ganzi flysch complex that outcrops widely throughout the region [e.g., *Weislogel*, 2008] (Figure 3). The flysch complex was significantly deformed by late Triassic folding and thrusting driven by collision and subsequent convergence between north and south China [Burchfiel *et al.*, 1995] to form the Kunlun suture. The Triassic flysch covers a broader area than simply the SG terrane, including regions north of the Kunlun suture where it rests on Paleozoic shallow marine sequences [Zhou and Graham, 1996] and regions south of the Jinsha suture where the flysch strata are interbedded with volcanoclastic rocks as deposits of a fore-arc basin [Yin and Harrison, 2000]. The Songpan-Ganzi flysch may have been deposited in a series of separate basins, most likely either ocean remnants [Yin and Nie, 1993] or back-arc basins north of a north dipping subduction zone along the Jinsha suture [Yin and Harrison, 2000].

### 2.2. East Kunlun Mountains

[9] On the north side of the SG terrane, the Kunlun Suture brings the SG flysch into contact with the East Kunlun Mountains, the southern part of the Kunlun-Qaidam terrane. Burchfiel *et al.* [1989] were one of the first groups to propose the EKM were uplifted by motion on a major north vergent thrust at the KQB, the North Kunlun Thrust (NKT). A north

vergent NKT has not been mapped at the surface (most portions of the KQB are covered by Quaternary fan deposits), but is an inferred buried thrust. *Mock et al.* [1999] suggest northward thrusting is caused by vertical wedge extrusion since 20–30 Ma to accommodate continental collision. *Meyer et al.* [1998], *Tapponnier et al.* [2001], and *Jolivet et al.* [2003] suggest that left-slip deformation dominates the region and that the EKM are a large transpressional system. *Chen et al.* [1999] use focal mechanisms and earthquake depths to support the presence of a south dipping thrust beneath the EKM, and *Song and Wang* [1993] interpret seismic reflection data to show syndepositional, fault-propagation folding associated with a north verging listric thrust at the KQB. *Bally et al.* [1986] interpret seismic reflection data to show north vergent thrust faults cutting through the lower Pliocene strata in south Qaidam, with north tilting and southward onlap of Middle Pliocene and later beds. A competing hypothesis based on field mapping at deep canyon exposures, satellite data analysis, and (mostly unpublished) seismic reflection data from west Qaidam suggests that the KQB area is dominated by Cenozoic south vergent thrusting [Yin *et al.*, 2007].

[10] The Eastern Kunlun Range was intruded by two phases of plutonism, together known as the Kunlun Batholith [Cowgill *et al.*, 2003]. Rifting in the Kunlun region during the Ordovician-Silurian caused widespread intrusions into Precambrian gneiss and Neoproterozoic metasediments. The localized, later episode of Permian-Triassic volcanism was caused by subduction. *Roger et al.* [2003] claim that late Triassic subduction was north dipping beneath the Kunlun based on the relative positions of granites, ultramafics, and flysch rocks. Others suggest that Permian-Triassic volcanism was precipitated by south dipping subduction of the South Qilian terrane beneath the KQ [Meyer *et al.*, 1998; Yuan *et al.*, 2010]. The Late Ordovician to Early Carboniferous marine sediments, and Jurassic and Cenozoic continental rocks, were deposited after each intrusive phase [Mock *et al.*, 1999].

### 2.3. Qaidam Basin

[11] The Qaidam Basin is the largest basin inside the Tibetan Plateau, located on the north side of the EKM with its long axis trending west-northwest. The contact between the Qaidam Basin and the East Kunlun Mountains (KQB) forms the most extensive topographic front (>1000 km long) and the largest relief (~2.5 km on average) inside the Tibetan plateau [Yin *et al.*, 2007]. The QB is bound in the north by the Cenozoic Qilian Shan-Nan Shan thrust belt and in the west by the left-lateral Altyn Tagh Fault (Figure 1). The Qaidam Basin contains an Eocene to Quaternary sedimentary sequence ranging in thickness from <3 km near the margins to >15 km near the center [Yin *et al.*, 2008a]. Hence the Qaidam Basin cannot be a simple foreland basin in front of the EKM, as such a basin would have a sedimentary sequence thickening southward toward the EKM [Bally *et al.*, 1986].

[12] Qaidam basement may consist of remnants of Late Proterozoic to Early Paleozoic metamorphic rocks, flysch, and carbonate [Wang and Coward, 1990]. Uplift of orogenic belts north and south of the Qaidam during the late Triassic or Jurassic led to deposition of foreland basin sediments [Xia *et al.*, 2001]. No known deposition occurred during most of the Cretaceous, and then a rift basin developed during the

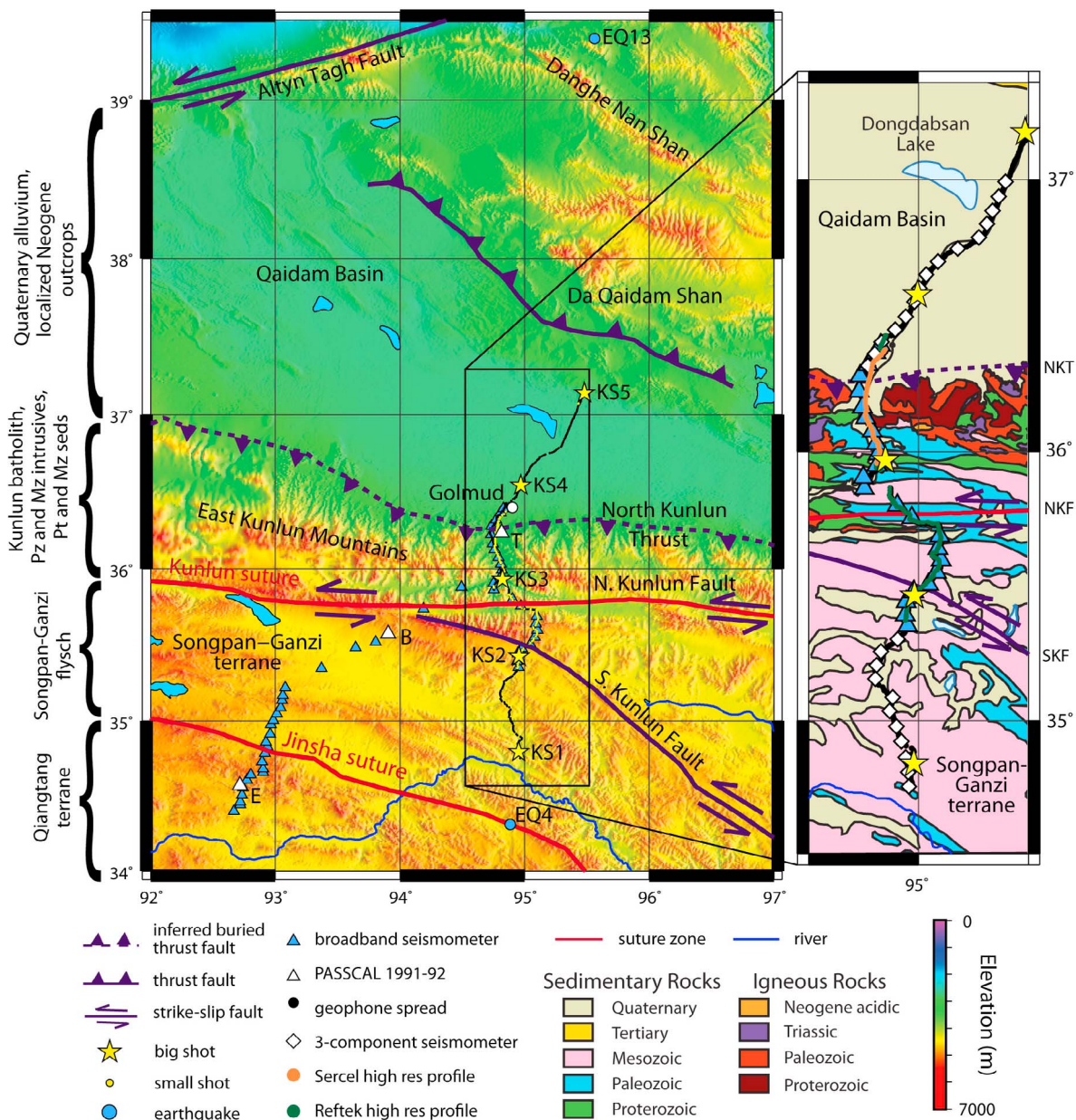


**Figure 3.** INDEPTH IV active source profile with faults and sutures overlain on the topography. (right) The receiver spreads are shown in greater detail superimposed on the geologic map [Pan et al., 2004]. SKF, South Kunlun Fault; NKF, North Kunlun Fault; NKT, North Kunlun Thrust.

late Cretaceous and early Tertiary and Cenozoic. This basin subsequently experienced intense compression during the Miocene and Pliocene arguably owing to remote propagation of compression from the India-Asia collision [Xia et al., 2001].

[13] Cross-section restorations based on seismic reflection interpretations have led to a total estimated maximum Cenozoic shortening of as little as 10 km [Zhou et al., 2006], or, using different thrust fault geometries and different amounts of thrust-related folding, as much as 70–80 km of Cenozoic shortening [Yin et al., 2008b], across the western QB.

**2.4. Active Kunlun Fault**

[14] The E-W to WNW-ESE trending left-lateral, strike-slip Kunlun Fault spans 1600 km of the zone of weakness associated with the Paleozoic Kunlun suture [Kidd and Molnar, 1988; Bian et al., 2004]. Though the timing of initiation of faulting is debated, several recent studies [Meyer et al., 1998; Jolivet et al., 2003; Fu and Awata, 2007] suggest faulting began ~10 Ma on the basis of mapping of rocks with total slip up to ~100 km combined with Quaternary slip rates of ~10–20 mm/yr from GPS [Wang et al., 2001; Zhang et al., 2004], field observations [Yin et al., 2008b; Harkins

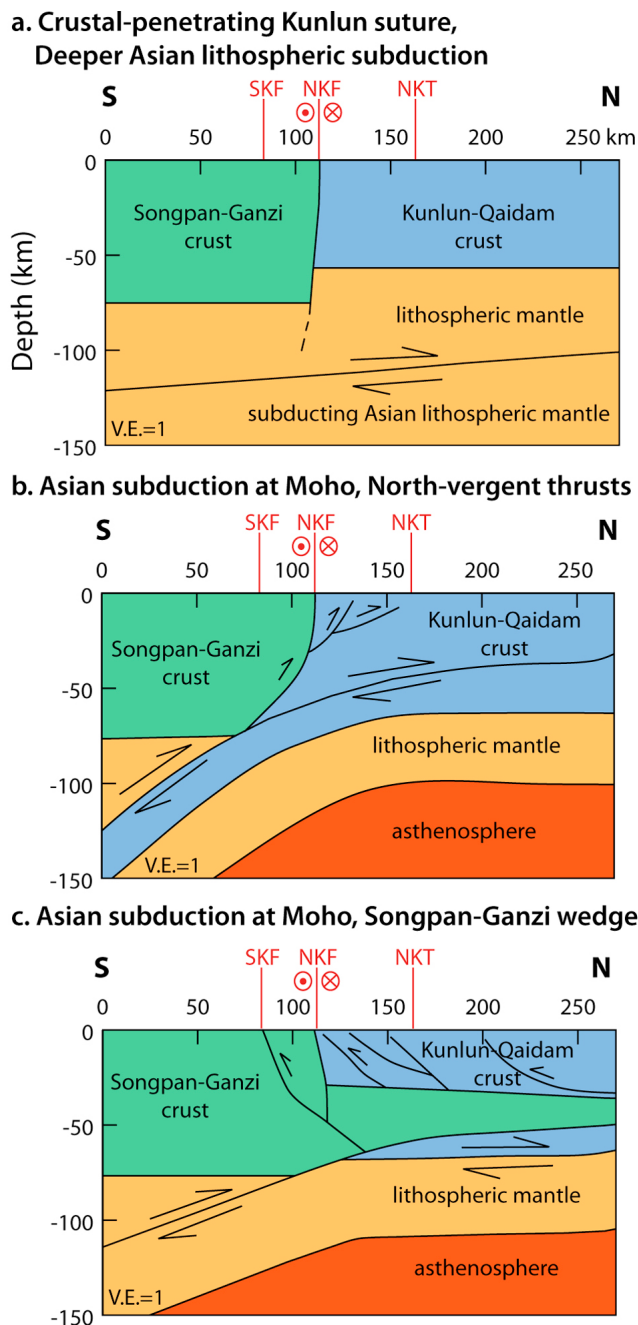


**Figure 4.** Cartoons redrawn after published models of active tectonics at the Kunlun suture. (a) Crustal-penetrating North Kunlun Fault (NKF) bringing thinner Kunlun-Qaidam crust in contact with thicker Songpan-Ganzi crust [e.g., *Tapponnier et al.*, 2001; *Li et al.*, 2011]. A deeper Asian lithospheric mantle slab is shown subducting to the south [*Kind et al.*, 2002]. (b) South directed Asian subduction at the Moho beneath the NKF and north vergent upper crustal thrust faults [*Meyer et al.*, 1998; *DeCelles et al.*, 2002]. (c) Songpan-Ganzi wedge indents Kunlun-Qaidam crust, with south directed Asian subduction at the Moho beneath the NKF (Kunlun suture) and south vergent upper crustal thrust faults [*Yin et al.*, 2007]. SKF, South Kunlun Fault; NKT, North Kunlun Thrust. V.E. is vertical exaggeration.

*et al.*, 2010], and satellite remote sensing [*Fu and Awata*, 2007]. At the longitude of our seismic profile the active Kunlun Fault is split into two branches (our SKF and NKF; see Figure 3) with SG terrane material between the branches. The Kunlun Fault has produced five  $M > 7.0$  earthquakes in the past century, most recently the M8.1 Kokoxili quake on 11/14/2001 that produced a 430 km surface rupture, reaching within about 10–20 km of the INDEPTH IV profile [*Fu et al.*, 2005]. The hypocenter depth is estimated at 17 km [*Lin et al.*, 2003], and the fault plane is thought to dip steeply south at 80–85° [*Lin et al.*, 2003; *King et al.*, 2005]. Thus we draw the NKF as a steeply south dipping fault (see Figure 13).

## 2.5. Previous Geophysical Data

[15] Previous seismic studies suggest an abrupt decrease in crustal thickness from the EKM to the QB [*Zhu and Helmberger*, 1998]. Data from two Chinese deep refraction profiles collected along the Golmud-Lhasa Highway (coincident with the northern part of our profile) show a Moho step from ~61 km beneath the EKM to ~52 km beneath the QB around the surface location of the KQB or NKT [*Li et al.*, 2004]. However, the geometry of these two profiles is not ideal to delineate the precise geometry of a Moho step around the NKT as the southern of the two profiles ended at Golmud just 20 km north of the NKT (Figure 3) and the northern of the two profiles had its southernmost shot point at Golmud and only a few recordings south of Golmud.

[16] About 400 km east of our INDEPTH IV profile, along the east Qaidam and Gonghe-Yushu profiles (Figure 1), *Jiang et al.* [2006] found the crust beneath the EKM and SG terrane to be about 72 km thick, but the QB crust to be 54 km thick. They interpret a southward dipping, continuous Moho with no abrupt Moho steps beneath this margin. About 550–600 km southeast of the INDEPTH IV profile, both the Darlag-Lanzhou-Jingbian profile [*Liu et al.*, 2006] and the Moba-Guide profile [*Zhang et al.*, 2011] also show no Moho step associated with the Kunlun suture. *Zhu and Helmberger* [1998] interpret double-pulse teleseismic  $P$  wave arrivals at a single station (TUNL; see Figure 1) in the foothills of the East Kunlun Mountains to argue for a 15 to 20 km Moho offset occurring over a narrow lateral range of less than 5 km near the NKT. *Vergne et al.* [2002] imaged a Moho offset of 10–12 km (from 70 km beneath the EKM to ~58 km in the QB) about 100 km north of the NKF (30 km north of the NKT) using teleseismic receiver functions from the Sino-French [Wittlinger *et al.*, 1996] and Program for Array Seismic Studies of the Continental Lithosphere (PASSCAL) [*Owens and Zandt*, 1997] experiments along the Golmud-Lhasa Highway. *Shi et al.* [2009] imaged a Moho offset of about 15 km (from ~70–63 km below land surface beneath the EKM to ~47 km beneath the land surface in the Qaidam Basin) using teleseismic receiver functions several hundred kilometers east of the INDEPTH IV profile (~98°E).

[17] Previous tectonic interpretations of the boundary between the high Tibetan Plateau and the Qaidam Basin have suggested a crustal-penetrating strike-slip zone at the NKF with minimal subduction [*Unsworth et al.*, 2004; *Chung et al.*, 2005; *Li et al.*, 2011] (Figure 4a) or southward subduction of Qaidam Basin crust beneath Tibet [*Meyer et al.*, 1998; *Yin and Harrison*, 2000; *Tapponnier et al.*, 2001; *Yin et al.*, 2008b] (Figures 4b and 4c) near the location of the NKF, despite the teleseismic data analyses that suggest the

crustal thickening from the Qaidam Basin southward to the Tibet Plateau occurs on a Moho step north of the NKF [Zhu and Helmberger, 1998; Vergne *et al.*, 2002]. We show below that south directed subduction of Qaidam lower crust beneath Tibet as a direct cause of the crustal thickness change between these provinces is incompatible with the geometry of wide-angle reflections observed during INDEPTH IV profiling. However, a deeper subduction of Asian crust beneath the East Kunlun Mountains [Kind *et al.*, 2002; Zhao *et al.*, 2010] is still possible (Figure 4a).

### 3. Data Acquisition and Inversion

#### 3.1. Seismic Acquisition

[18] The INDEPTH IV Kunlun active source seismic profile is 270 km long and trends roughly S-N from the Songpan-Ganzi terrane at higher elevation in the south to the Qaidam Basin in the north. The profile employed three different types of receiver spreads (Figure 3):

[19] 1. Near-vertical (NV) deployment consisting of 655 Reftek RT125 PASSCAL “Texan” recorders at 100 m spacing with 4.5 Hz geophones and a 1000 channel Sercel cabled spread with 50 m spacing and arrays of 4.5 Hz geophones across the central portion of the profile (including the SKF, NKF, and NKT).

[20] 2. Wide-angle (WA) deployment of 295 Texan recorders with 4.5 Hz geophones at 650 m spacing along the entire 270 km profile.

[21] 3. Three component (3C) array (48 Geophysical Instrument Pool Potsdam and SEIS-UK short-period and broadband instruments at 5–6 km spacing) along the entire 270 km profile.

[22] Seismic sources included five large explosive shots named KS1, KS2, KS3, KS4, and KS5 (south to north) roughly evenly spaced along the profile containing 2000, 1500, 1000, 1500, and 2000 kg of seismic explosives, respectively. There were 105 small shots, each 60–240 kg explosive, at nominal 1 km spacing along the central portion of the profile. An additional small shot (9119) was 8 km south of KS5. Large shots were fired using multiple boreholes, loaded with no more than 100 kg of explosive. The large-shot geometry was designed to image the entire crust, with particular interest in wide-angle reflections from the crust-mantle boundary (Moho). The small-shot geometry was designed to image detailed structure near the SKF, NKF, and NKT.

[23] The INDEPTH IV passive seismic experiment deployed 59 broadband stations (24 of which were along the Kunlun profile; see Figure 3) from May 2007 to September 2008 [Zhao *et al.*, 2008]. Except for ray tracing of two local earthquakes, the 3C and broadband data analyses are left to other studies [Mechie *et al.*, 2007].

[24] In this paper, we analyze the vertical component, *P* wave recordings for the active source explosions. Data quality is good for about 86% of Texan recordings. The other 14% were noisy or had unclear signals likely owing to anthropogenic noise, instrument malfunction, or wind noise. Broadband recordings from two earthquakes (Figure 3) provided additional constraints on Moho structure and upper mantle velocity in our velocity models. A M3.9 earthquake (EQ4) on 18 November 2007 was relocated using stations from the INDEPTH IV linear and areal broadband arrays [Wei

*et al.*, 2010]. A M4.7 earthquake (EQ13) on 16 July 2008 could not be relocated owing to poor station coverage in north Qaidam, and the location was taken from the USGS PDE catalog.

#### 3.2. Data Processing

[25] Texan and Sercel recordings were resampled at 8 ms and merged into shot gathers, and a Butterworth zero-phase frequency band-pass filter of 2 to 18 Hz (filter low- and high-cut slopes 14 and 72 dB per octave) for the Texans and 4 to 18 Hz (12 and 72 dB per octave) for the Sercel improved signal-to-noise ratio. Other attempts to filter anthropogenic noise along the northern 80 km of the profile were largely unsuccessful.

[26] Figure 5 shows reduced traveltime record sections from the five large shots, Figure 6 shows a shot gather for large shot KS5 displayed as a single-fold reflection section, and Figure 7 shows the two earthquake records. Nine seismic phases were recognized and picked in record sections for the 5 large shots and 105 small shots and then used in *P* wave modeling. The clearest arrivals, mainly near-offset first arrivals, were assigned a traveltime uncertainty of  $\pm 0.05$  s, a conservative estimate based on a qualitative estimate of the first-arrival signal-to-noise ratio. The least-clear first arrivals and reflections were assigned a traveltime uncertainty of  $\pm 0.2$  s.

[27] The first phase, the upper crustal refraction, *P<sub>g</sub>*, is observed in the record sections from all shots. The near-surface *P<sub>g</sub>* velocities are low beneath the Qaidam Basin (2.2–2.5 km/s), higher beneath the Songpan-Ganzi terrane (4.5–5 km/s), and highest beneath the East Kunlun Mountains (>5 km/s). The large-shot source gathers show clear first arrivals out to offsets ranging from 130 to 200 km. The main branch of *P<sub>g</sub>* has average apparent velocity of about 6 km/s for most shots. *P* wave propagation is better to the south than the north owing to high attenuation by up to 3 km Quaternary sediments [Yin *et al.*, 2008b] and Tertiary sedimentary rocks in the Qaidam Basin as well as anthropogenic noise from the highway and Golmud city.

[28] In addition to the first arrivals, the 5 large shot gathers and 2 local earthquakes in line with the profile show modeled arrivals for seven reflected phases, *Pi1P*, *Pi2P*, *Pi3P*, *Pi4P*, *Pi5P*, *Pi6P*, and the Moho reflection, *PmP*. Table 1 displays the lateral distance range on the shot gathers (Figures 5, 6, and 7) over which each reflection or refraction phase was picked for each large shot and earthquake. The prominent reflectors south of the East Kunlun Mountains are *Pi1P* at  $\sim 14$  km depth (from KS2), *Pi2P* at  $\sim 20$  km depth (from KS3), *Pi4P* at  $\sim 35$  km depth (from KS1, KS3, KS4), *Pi6P* at  $\sim 50$  km depth (from KS3, KS4), and *PmP* at  $\sim 62$ – $70$  km depth (from KS3, KS4, KS5, EQ4) (Figures 5, 6, and 7). The most prominent reflectors north of the East Kunlun Mountains are *Pi2P* at  $\sim 20$  km depth (from KS4), *Pi3P* at  $\sim 30$  km depth (from KS4), *Pi5P* at  $\sim 42$  km depth (from KS4), and *PmP* at  $\sim 52$  km depth (from KS4, KS5) (Figures 5 and 6) beneath the Qaidam Basin. The Moho structure beneath the Qaidam Basin is also constrained by the mantle refraction, *P<sub>n</sub>* (from EQ13) (Figure 7). See Appendix A for the raw large-shot and earthquake data with no superimposed interpretations. Given the significant terrane boundaries crossed by our profile, wide-angle reflectors at similar depths may not represent the same structural feature. No mantle refractions were recorded

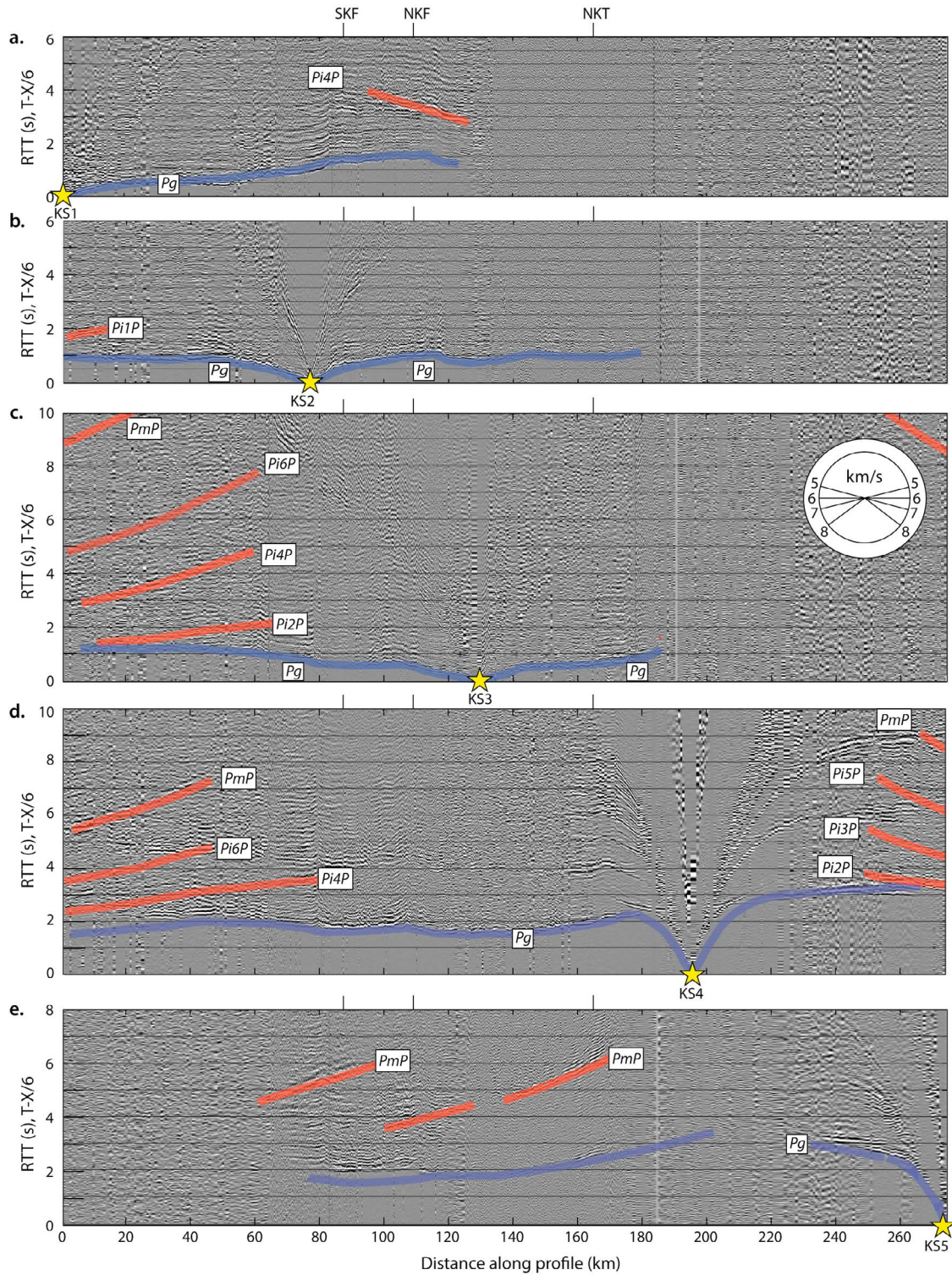


**Figure 5.** Large shot gathers displayed in reduced traveltimes with model refraction/reflection phases for (a) KS1, (b) KS2, (c) KS3, (d) KS4, and (e) KS5. Blue curves are model-calculated traveltimes from first-arrival tomography. Red curves are model-calculated traveltimes from reflection ray tracing. Curves are only displayed in the vicinity of actual data picks. Velocity wheel in Figure 5c gather shows slopes of arrivals of velocities from 5 to 8 km/s. SKF, South Kunlun Fault; NKF, North Kunlun Fault; NKT, North Kunlun Thrust.

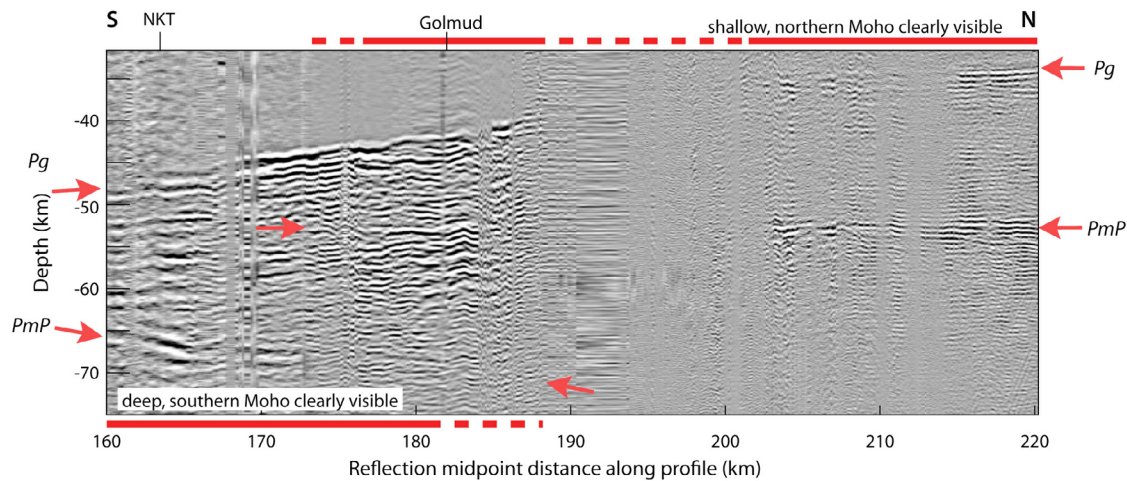


**Figure 6.** Shot gather for KS5 displayed as single-fold midpoint reflection section after correction for normal moveout and depth conversion using 6.2 km/s average velocity and a datum of 4800 m. Distance of source-receiver midpoints is indicated along the bottom of the section. Energy arriving before the Moho reflections ( $PmP$ ) corresponds to direct  $P$  phases ( $Pg$ ) and associated multiples. Solid red lines indicate areas where Moho reflections are clearly visible; dashed red lines indicate areas where Moho reflections are less clear. Arrows point to the lateral extents of the reflection picks. NKT, North Kunlun Thrust.

from the large shots because the Moho was too deep relative to the largest source-receiver offset.

### 3.3. Traveltime Tomography

[29] Our traveltime modeling incorporated a top-to-bottom approach. First, tomographic inversion of 21,525 first-arrival picks for the 105 small shots and 5 large shots constrained the shallow structure down to 20 km using the ray-tracing technique detailed by Cervený *et al.* [1977]. Then deeper layers were added to the model, and forward ray tracing with RAYINVR [Zelt and Smith, 1992] was used to constrain the reflector depths and whole crustal velocity structure.

#### 3.3.1. Shallow Velocity Inversion

[30] Using a modified version of Cervený's code, traveltimes were forward modeled using finite difference ray tracing based on the eikonal equation [e.g., Vidale, 1988]. The model used an irregular  $77 \times 10$  grid (shown in Appendix B; see Figure B2) with the finest spacing across the central, better sampled portion of the profile (the smallest cells are 2 km wide and 1 km deep). The starting model (initial velocity grid) was created on the basis of 1-D models along the profile from basic trial-and-error forward ray tracing of both large and small shots and, in the Qaidam Basin, previous velocity models of that area [Jiang *et al.*, 2006; Zhao *et al.*, 2006]. Partial derivatives of the calculated traveltimes with respect to the velocity grid nodes were then computed [Lutter *et al.*, 1990]. A damped least squares inversion utilizing the LSQR variant of the conjugate gradient method [Paige and Saunders, 1982] was used to update the velocity nodes, and the forward and inverse problems were repeated until an acceptable convergence between the observed and calculated traveltimes was obtained. The final iteration RMS error is 0.11 s, close to the estimated uncertainty of our traveltime picks, so an acceptable result.

[31] A second, finer grid of  $170 \times 19$  nodes (minimum cell size 1 km distance by 0.5 km depth) converged to an RMS error of 0.13 s, and only the  $77 \times 10$  node model is shown here

(Figure 8b). The model-calculated traveltime curves for  $Pg$  of the five large shots are shown as blue curves in Figure 5. The ray coverage for the tomography extended down to a maximum depth of about 20 km and was best in the area of high receiver and shot density, the central 100 km of the profile (Figure 9a). Areas crossed by few or no rays (Figure 9a)

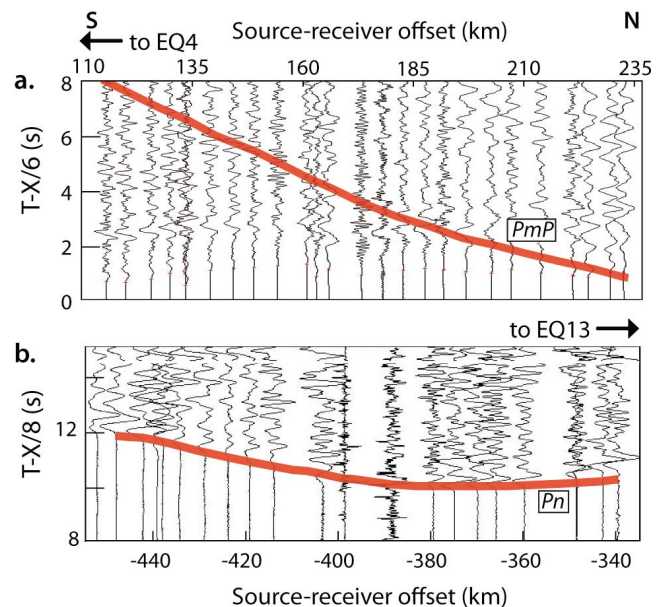


**Figure 7.** Earthquake records for (a) EQ4 and (b) EQ13 recorded on 24 broadband stations. Red curves are traveltimes for  $PmP$  (Figure 7a) and  $Pn$  (Figure 7b) calculated from ray tracing through our final model (Figure 8c). Trace locations are displayed relative to the earthquake-receiver offset. The x axes correspond to 60–185 km distance along the INDEPTH IV profile.

**Table 1.** Lateral Distance Range on the Shot Gathers Over Which Each Reflection or Refraction Is Observed for Each Large Shot and Earthquake Given as Distance Along the Profile<sup>a</sup>

	KS1 (km)	KS2 (km)	KS3 (km)	KS4 (km)	KS5 (km)	EQ4 (km)	EQ13 (km)
<i>Pi1P</i>		0–16					
<i>Pi2P</i>			10–65	248–270			
<i>Pi3P</i>				250–270			
<i>Pi4P</i>	95–125		0–57	0–80			
<i>Pi5P</i>				252–270			
<i>Pi6P</i>			0–55	0–43			
<i>PmP</i>			0–22	0–40; 265–270	60–95; 100–125; 136–170	60–185	
<i>Pn</i>							60–185

<sup>a</sup>See Figures 5 and 7.

are the least well resolved by the shallow tomography, as expected, however, many of these areas are further resolved by the deep reflection and refraction modeling (see section 3.3.2). See Appendix B for discussion of checkerboard and model recovery tests.

**3.3.2. Deep Reflection and Refraction Modeling**

[32] After obtaining the shallow velocity model, deeper layers were added. Velocity values at important structural locations along the profile were sampled from the smooth shallow tomographic model to create the layered velocity model. Layers were inserted where reflections were seen in the explosion records. To incorporate the earthquake sources

about 50 km off the south end and about 250 km off the north end of the profile, the model was expanded to a total length of 630 km. The velocity structure of the area north of the profile was based on previous studies [e.g., Meng et al., 1995].

[33] The initial model layer thicknesses were based on depth calculations from reflections in the shot gathers (*Pi1P*, *Pi2P*, *Pi3P*, *Pi4P*, *Pi5P*, *Pi6P*, and *PmP*) and earthquake records. Figure 8c shows with white lines only the segments of the reflectors that correspond to obvious signal in the data. Most of these reflectors almost certainly extend farther horizontally, but those signals are less clear (e.g., owing to noise, lack of station coverage, changes in impedance contrast along

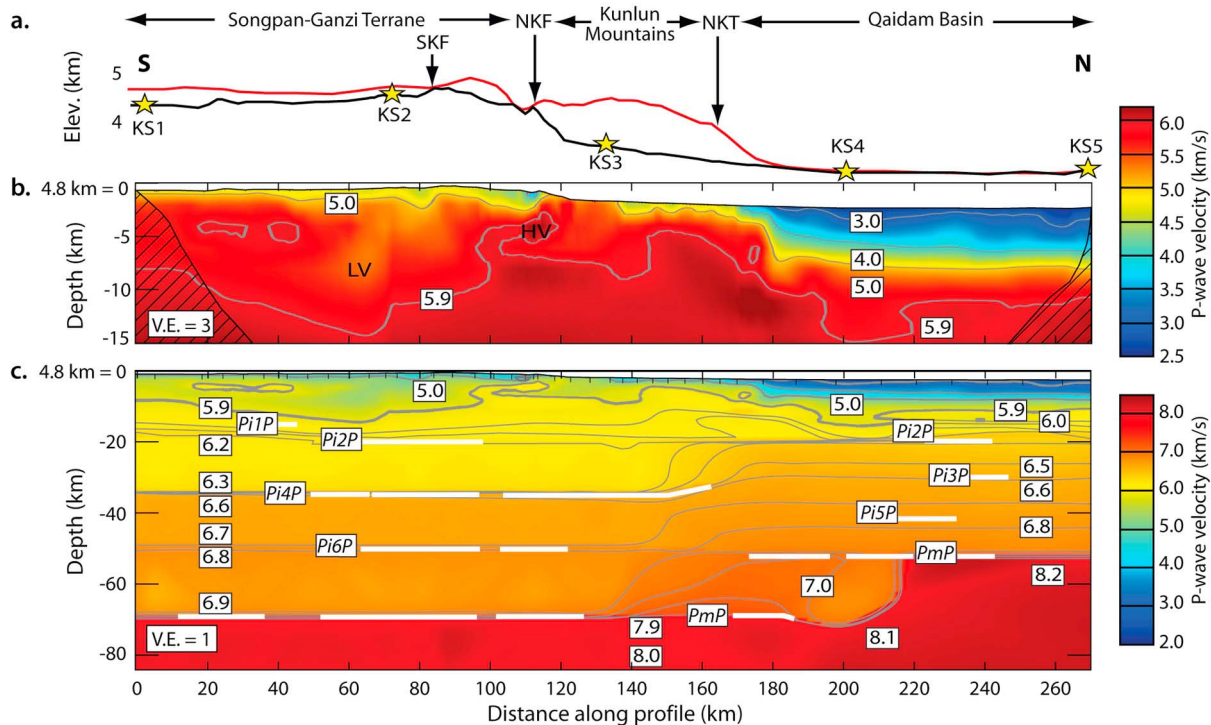


**Figure 8.** (a) Elevation measured along INDEPTH IV active source profile (black curve) and TOPO1 elevation along the INDEPTH IV profile averaged over longitudes from 94 to 96°E (red curve). SKF, South Kunlun Fault; NKF, North Kunlun Fault; NKT, North Kunlun Thrust. (b) Shallow crust velocity model from first-arrival tomography (color scale from 2.5 to 6.1 km/s). Zero depth is equivalent to 4.8 km elevation. Vertical exaggeration (V.E.) is three times. Striped area is unconstrained by first arrivals. LV, low-velocity region; HV, high-velocity region. (c) Composite shallow and deep crustal velocity model from ray tracing the INDEPTH IV controlled-source profile (color scale from 2.0 to 8.2 km/s). Major reflectors shown as white lines. No vertical exaggeration.

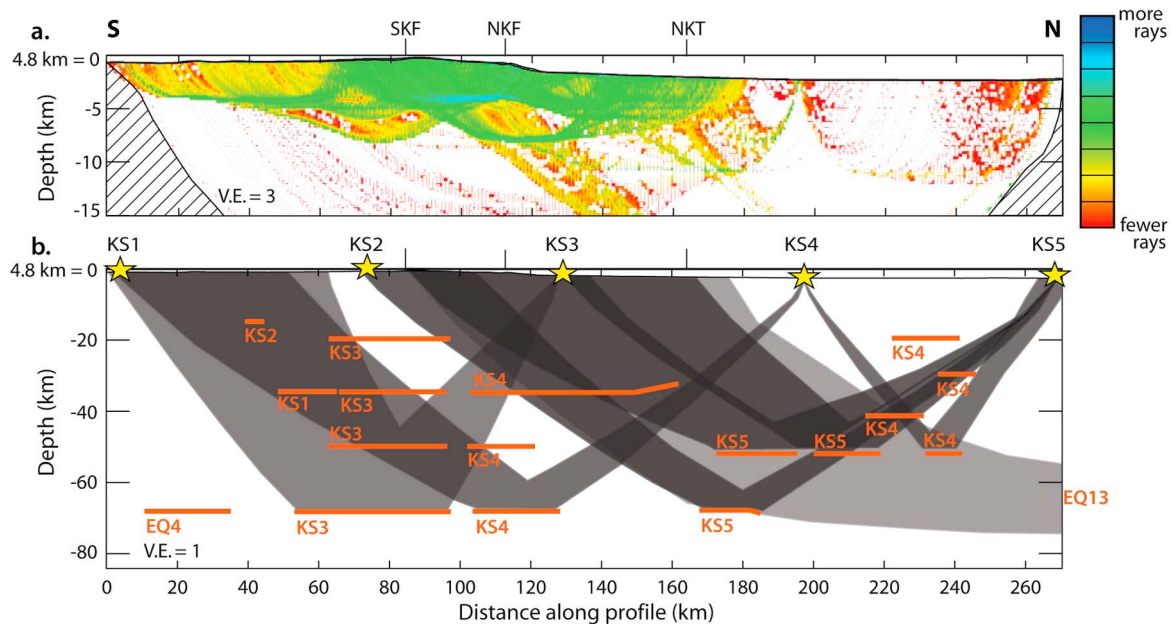


**Figure 9.** (a) Ray coverage used for shallow tomography (V.E. = 3). (b) Ray coverage used to constrain Moho structure from large shots KS3, KS4, and KS5 (shown as yellow stars) as well as EQ4 and EQ13 (located beyond the extents of the displayed area). Reflectors shown as orange lines. No vertical exaggeration. The name of the shot recording each reflection is shown by the reflector. SKF, South Kunlun Fault; NKF, North Kunlun Fault; NKT, North Kunlun Thrust.

the boundary, etc.). Stepwise velocity increases were incorporated across the reflectors. Reflection and  $P_n$  picks for the five large shots and two earthquakes were compared to 2-D ray tracing model-predicted outcomes using the RAYINVR code [Zelt and Smith, 1992] to model the eight ray groups.

[34] Iterative forward modeling with updated layer geometries and velocity values converged on a velocity model for the entire crust (Figure 8c). The model-calculated traveltime curves for the reflections of the five large shots are shown as red curves in Figure 5. Figure 9b displays the ray coverage used to determine the Moho structure from the earthquakes and large shots. The final shallow and deep velocity models are not unique solutions, but evaluation of the deviation between model and measured phase picks (error) indicates that models fit the data within reasonable error margins.

#### 4. Crustal Velocity Structure

[35] The velocity structure (Figure 8) was used to interpret thicknesses of key units, locations of intrusions, locations of faults, Moho structure, and types of rocks beneath each terrane and major tectonic feature.

##### 4.1. Velocity Model of the Songpan-Ganzi Terrane

[36] The SG terrane has near-surface velocities of 4.6–4.8 km/s (Figure 8b). Velocities increase to 5.7 km/s at about 10 km beneath the highest point of the profile, 4800 m (all “depths” quoted and displayed are referenced to this elevation). There is a slightly higher-velocity, 5.8–5.9 km/s, elliptical body laterally between KS1 and KS2 between 3 and 7 km depth that is underlain by lower velocities of about 5.5–5.6 km/s. This slightly higher-velocity body likely cor-

responds to one of the higher-velocity segments seen in the first arrivals ( $P_g$ ) of KS1 (Figure 5a).

[37] The SG flysch outcrops as slates and sandstone beds [Roger *et al.*, 2003] and elsewhere as greenschist-grade metaturbidites [Weislogel, 2008]. Compilations of laboratory measurements suggest that metagreywackes of zeolite-to-greenschist grade have seismic velocities of  $5.5 \pm 0.6$  km/s in the upper 10 km for typical geotherms [Christensen and Mooney, 1995]. In contrast, granitic gneiss has a seismic velocity of  $6.1 \pm 0.1$  km/s in the same depth and temperature range. Hence, we choose the 5.9 km/s isovelocity contour (shown in Figure 8b) as a proxy for the base of the SG flysch along our profile and interpret the upper 8–14 km of the southern part of our profile as SG flysch. Our flysch thickness is consistent with previous studies that have shown the SG flysch strata to have thickness  $>10$  km, with localized areas of 15 km thickness [e.g., Weislogel, 2008].

[38] The strongest reflector beneath the SG terrane is  $Pi4P$  at 35 km depth (Figure 8c) that has relatively high amplitudes in the KS1 record (Figure 5a). Other intracrustal reflectors are  $Pi1P$  at 14 km,  $Pi2P$  at 20 km, and  $Pi6P$  at 50 km depth (Figure 8c).

[39] The Moho depth is 70 km beneath 0–215 km based on the velocity of the Moho reflections from EQ4 (see Figures 7a, 8c, and 9b). Lower-crustal velocities range from 6.6 to 6.9 km/s, indicating intermediate composition material [Christensen and Mooney, 1995].

##### 4.2. Velocity Model Beneath the NKF, SKF, and East Kunlun Mountains

[40] Surface outcrops indicate that the SG flysch exists between the SKF and NKF. However, this region has a

thicker, near-surface, lower-velocity (<5 km/s) region compared to the SG terrane further south (reaching about 3 km depth below the surface), perhaps indicating fracturing of the flysch due to faulting. Two distinct, south dipping low-velocity zones reaching about 2–3 km depth are located just south of the known locations of the NKF and SKF. A more diffuse, apparently south dipping region of low velocities extends from the surface location of the SKF to about 20 km south and about 8 km depth subsurface (LV in Figure 8b). The NKF corresponds to a larger near-surface low-velocity anomaly, with the lowest velocity near the NKF of 3.8 km/s representing a roughly 15% reduction in  $V_p$ . Wang *et al.* [2009] show that  $P$  wave velocities are reduced by 7–20% in at least the upper 1–2 km beneath the NKF.

[41] Beneath the East Kunlun Mountains, just north of the NKF between about 115–135 km distance along the profile, near-surface velocities are highest (>5 km/s) north of the Mesozoic sedimentary rocks. Almost directly beneath the NKF at about 5 km depth is a roughly elliptical (5 km horizontal by 3 km vertical) high-velocity anomaly of 6.0–6.2 km/s that we interpret as an intrusion (HV in Figure 8b). Geological mapping (Figure 3) shows possibly analogous Paleozoic magmatic bodies along strike to the east and west. The 5.9 km/s contour is shallower in this area than elsewhere along the profile.

[42] The EKM middle and lower crust have similar velocities to the SG middle and lower crust (Figure 8c), that are ~0.1–0.2 km/s slower than velocities at the same depth beneath the QB. The lateral velocity gradient spans ~20 km immediately south of the NKT in our model (Figure 8c), though this gradient could occur over a narrower region in reality. Our modeling indicates a lateral change in middle- to lower-crustal velocities beneath this area but cannot resolve the difference between a lateral velocity change occurring over 20 km and one occurring over, for example, 5 km.  $Pi4P$  and  $Pi6P$  continue beneath the EKM, and the Moho also appears flat at 70 km.

#### 4.3. Velocity Model of the Qaidam Basin and NKT

[43] Undulating regions of high and low velocity (seen in the 5 km/s contour line in Figure 8b) extending to ~1–2 km subsurface depth near the southern border of the Qaidam Basin may represent thrust sheets of a thrust system at the NKT. If the NKT is north directed, the northern edge of the higher velocity, near-surface material seen at ~180 km may correspond to the southern extent of shallow thrust faulting bringing higher-velocity rocks over lower-velocity rocks.

[44] The Qaidam Basin between 180 and 270 km has low surface velocities of 2.2–2.8 km/s. Velocities of 2.2–3.5 km/s likely correspond to a 4 km thick package of Cenozoic sedimentary basin rocks. Velocities of 3.5–5.7 km/s from ~4 to 8 km depth subsurface indicate an ~4 km thick layer of Paleozoic to Mesozoic sedimentary rocks underlying the inferred Cenozoic fill.

[45] Upper and middle-crustal reflectors exist at 20 km ( $Pi2P$ ), 30 km ( $Pi3P$ ) and 42 km ( $Pi5P$ ). Qaidam upper crustal velocities between 10 and 20 km subsurface depth are 5.8–6.2 km/s, indicating felsic crustal material. Velocities are 6.4–6.7 km/s in the middle crust and 6.7–6.9 km/s in the lower crust, corresponding to intermediate composition material.

[46] The crustal thickness changes by 18 km in the south Qaidam Basin, between 195 and 215 km. Figure 6 shows a depth-converted single-fold shot gather displayed in mid-point coordinates for northernmost large shot KS5. The south part of this gather shows a strong reflection from 160–185 km, which we ray trace to be from 70 km depth, the same depth as the Moho reflection further south beneath the EKM and SG. There is also a deep reflection in the north which we ray trace to be at 52 km depth, visible between 180 and 190 km, lost in the noisy region between 190 and 200 km, and strongest between 200 and 220 km. This reflection is from the same depth as our 52 km Moho reflections between 225 and 245 km from shots KS4, KS5, and 9119. These ray-trace depths derived using the full 2-D velocity-depth model are more accurate than the reflection depths in Figure 6 derived assuming a constant velocity.

[47] The reflection traveltimes combined with the raypath geometry from shot point KS5 require the existence of crustal velocity (6.6–7.2 km/s) material between 52 and 70 km depth extending about as far north as 210 km. Rays from KS5 to the 70 km reflector travel through the rectangular region between lateral 188–210 km and depth 52–70 km and their traveltimes can only be fit with crustal velocity material in this region, extending 40 km north of the northern visible extent of the 70 km reflector. Figure 9b shows that the location of the change in crustal thickness is additionally constrained by EQ13. Hence 70 km crust extends almost 100 km north of the NKF and 45 km north of the NKT. The presence of crustal velocity (<7.2 km/s) material between the strong 52 and 70 km reflectors suggests a “double Moho” in this area.

[48] We tested the sensitivity of our velocity model to uncertainties in the location of EQ13. Our basic Moho structure, including the spatial overlap of the Qaidam and Kunlun Moho reflections, is supported for likely hypocentral uncertainty ( $\pm 5$  km in latitude,  $\pm 3$  km in depth), but the northern margin of the crustal velocity material below the Qaidam Moho could move north or south by 10 km.

#### 5. Bouguer Gravity Analysis

[49] We tested our seismic velocity model against a Bouguer gravity anomaly profile along the Golmud-to-Lhasa highway, that we extracted from gridded and contoured data from the Tibet Global Geoscience transect [Wu *et al.*, 1991; Meng *et al.*, 1995]. This gravity profile follows the INDEPTH IV profile north of large shot KS3 and then deviates from the INDEPTH IV profile south of KS3 to follow the highway up to 200 km west of our seismic profile.

[50] We converted our model velocities (Figure 8c) to densities using a polynomial regression fit to the Nafe-Drake curve [Brocher, 2005]:  $\rho(\text{g/cm}^3) = 1.6612V_p - 0.4721V_p^2 + 0.0671V_p^3 - 0.0043V_p^4 + 0.000106V_p^5$ . We then simplified the model into blocks associated with density anomalies relative to the EKM middle crust, and modeled gravity predicted for those densities (Figure 10). Overall the density model derived from the  $P$  wave velocity model produced theoretical gravity values remarkably well aligned with the observed gravity data. The high-velocity anomaly beneath the EKM (HV in Figure 8b) corresponds to a positive Bouguer anomaly, presumably from the high-density Kunlun batholith and metamorphic rocks in the mountains. The low velocities (and densities) beneath the QB and fault zones correspond to

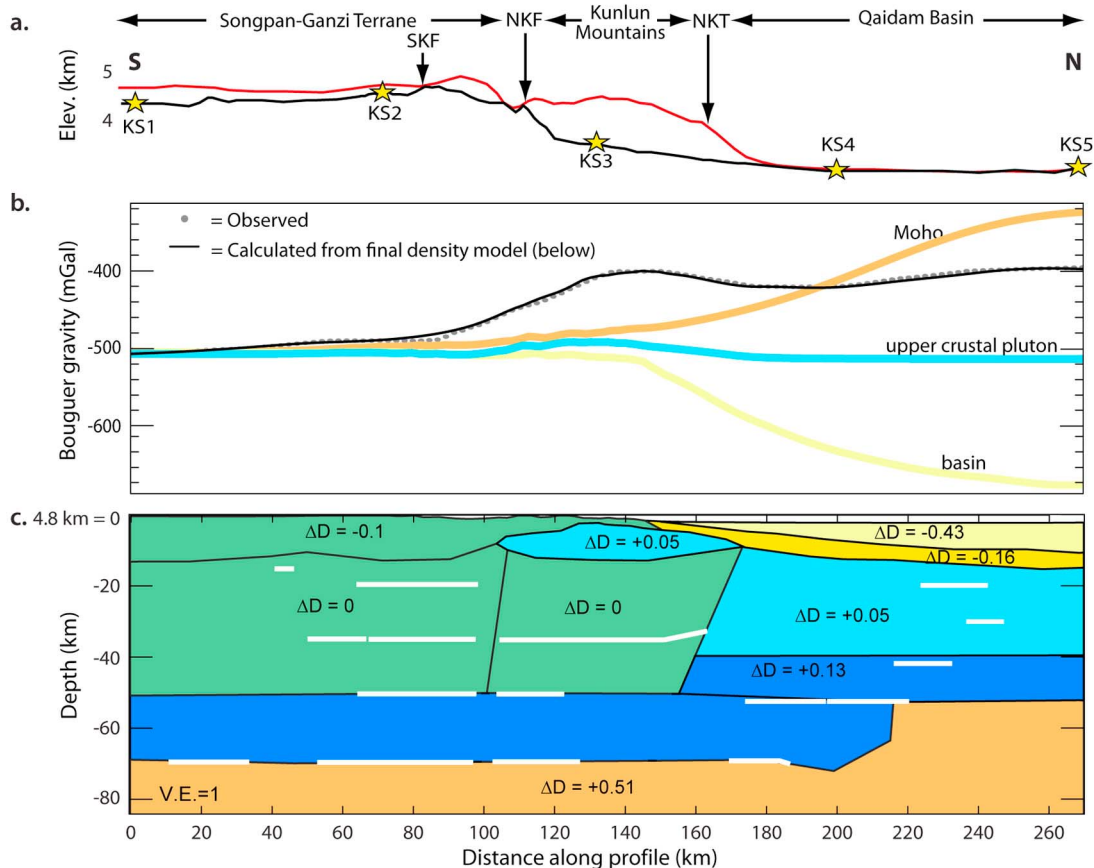


**Figure 10.** (a) Elevation along INDEPTH IV, as in Figure 8a. (b) Bouguer anomaly data (gray dots) from the Tibet Global Geoscience Transect [Wu *et al.*, 1991; Meng *et al.*, 1995] plotted with a calculated gravity curve (thin black line) for the model shown in Figure 10c. Colored curves isolate the effects of the Moho (orange), upper crustal pluton (blue), and Qaidam Basin (yellow). (c) Density model derived from the velocity model in Figure 8c used for gravity modeling in Figure 10b. White lines are reflectors mapped in Figure 8c.

negative Bouguer anomalies. The QB has the highest-velocity (and density) middle crust, and the middle crust velocity (and density) decreases beneath the EKM and SG. The location of the Moho step cannot be moved north or south more than  $\pm 10$  km, unless the shallow densities, converted from the shallow velocities that are the best constrained part of the velocity model, are also changed (see Appendix C).

## 6. Tectonic Implications

### 6.1. Comparison With Previous Tibet Velocity Models

#### 6.1.1. Active Source Velocity-Depth Curves

[51] We compared our new velocity models with previous models from the SG, EKM, and QB as well as other terranes of Tibet and the global average velocity curves for the continental crust [Christensen and Mooney, 1995] and oceanic crust [White *et al.*, 1992]. All our 1-D velocity-versus-depth ( $v$ - $z$ ) curves are laterally averaged over a few tens of kilometers and are referenced to the local ground surface. Figure 11a compares  $v$ - $z$  curves for the SG terrane from this study (laterally averaged over locations 50–100 km along the profile), the Gonghe-Yushu profile [Jiang *et al.*, 2006], the Moba-Guide profile [Zhang *et al.*, 2011], the Darlag-

Lanzhou-Jingbian profile [Liu *et al.*, 2006], and the global average continental and oceanic crust curves. Our SG velocity profile falls at and below the lower  $1\sigma$  bound of the average crustal velocity curve at most depths and the crustal thickness is about 20 km greater, as expected for an active orogen. The four SG curves are broadly similar, probably within likely uncertainties and spatial variations, except for variable crustal thicknesses of 62 to 70 km and the high-velocity zone between 35 and 40 km depth seen only in the Jiang *et al.* [2006] curve. The two westernmost SG curves from this study and the Gonghe-Yushu profile have  $\sim 70$  km crust, then the crust appears to thin to the east with 64 km crust along the Moba-Guide profile and 62 km crust along the Darlag-Lanzhou-Jingbian profile. Jiang *et al.* [2006] added the high-velocity zone to their model in order to better fit the data amplitudes. All four SG curves have relatively low velocities in the lower crust ( $< 7$  km/s), permissive of felsic lower-crustal material or partial melts. Many tectonic models [e.g., Yin and Nie, 1993] assume that the Songpan-Ganzi flysch was initially deposited on oceanic crust, but such a crust when buried to any significant depth should be characterized, over a thickness of at least 5 km, by velocities exceeding 7 km/s [White *et al.*, 1992]. Whether or not the

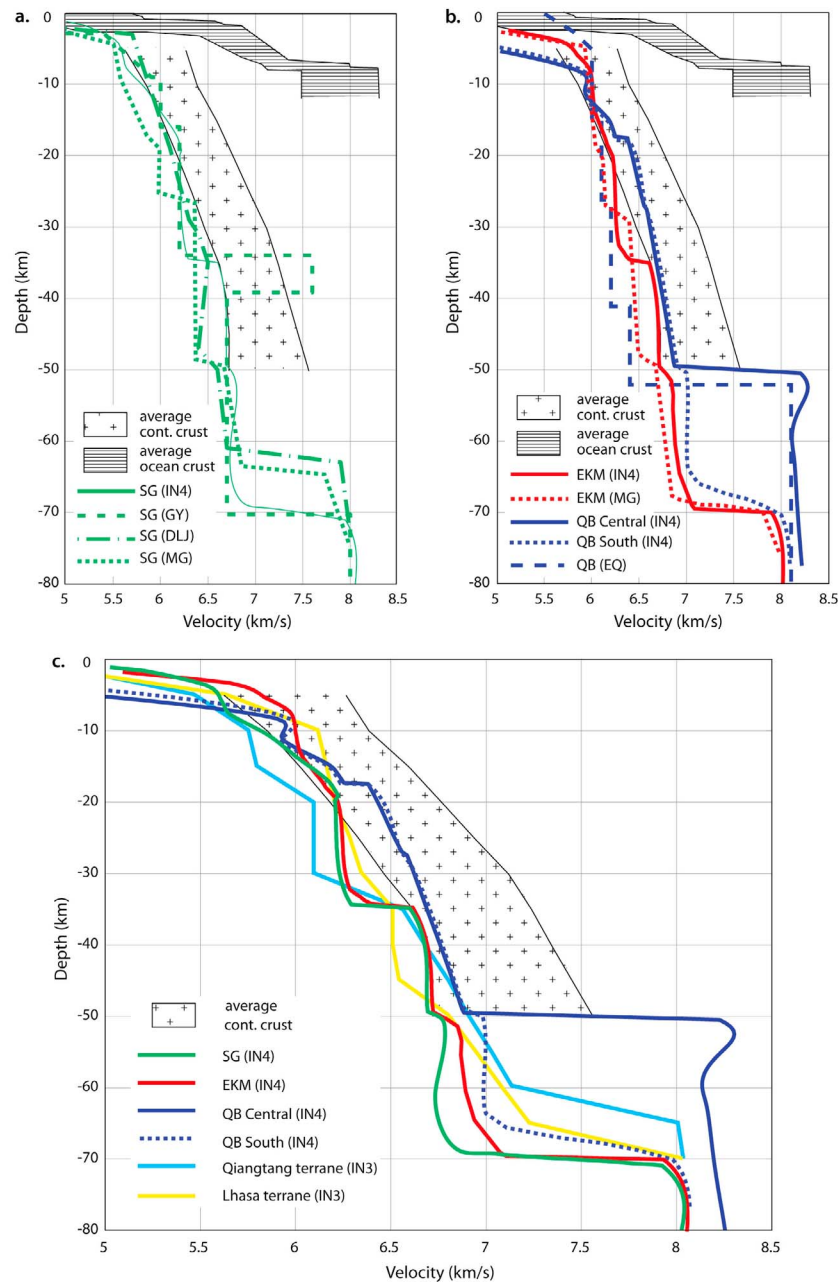


**Figure 11.** (a) Comparison of INDEPTH IV (IN4) Songpan-Ganzi terrane (SG) average 1-D velocity model with those from the Gonghe-Yushu profile (GY), the Darlag-Lanzhou-Jingbian profile (DLJ), and the Moba-Guide profile (MG) (see Figure 1). (b) Comparison of IN4 East Kunlun Mountains (EKM) and Qaidam Basin (QB) 1-D velocity models with those from the east Qaidam profile and MG (see Figure 1). (c) Comparison of IN4 SG, EKM, and QB models with Qiangtang and Lhasa terrane models (from the INDEPTH III profile) [Zhao *et al.*, 2001]. Patterned regions in each plot represent  $1\sigma$  bounds on the average continental and oceanic crustal velocities [White *et al.*, 1992; Christensen and Mooney, 1995].

Songpan-Ganzi flysch was originally deposited on oceanic crust, at the longitude of our profile ( $95^{\circ}\text{E}$ ), as elsewhere in NE Tibet [Zhang *et al.*, 2011], it is now underlain by continental crust.

[52] Figure 11b compares our laterally averaged  $v$ - $z$  curves for the East Kunlun Mountains (120–160 km), southernmost Qaidam Basin (170–210 km), and central Qaidam Basin (220–250 km) with results from the east Qaidam profile

[Jiang *et al.*, 2006] and the Moba-Guide profile [Zhang *et al.*, 2011] (Figure 1). In the top 8 to 10 km the QB curves have lower velocities than the EKM, as expected owing to the low-velocity basin. Our QB curves lie squarely within the range of average continental crust, with middle- and lower-crustal velocities higher than those in the EKM. The east Qaidam profile  $v$ - $z$  curve has significantly lower middle- and lower-crustal velocities than our QB curves, perhaps because their

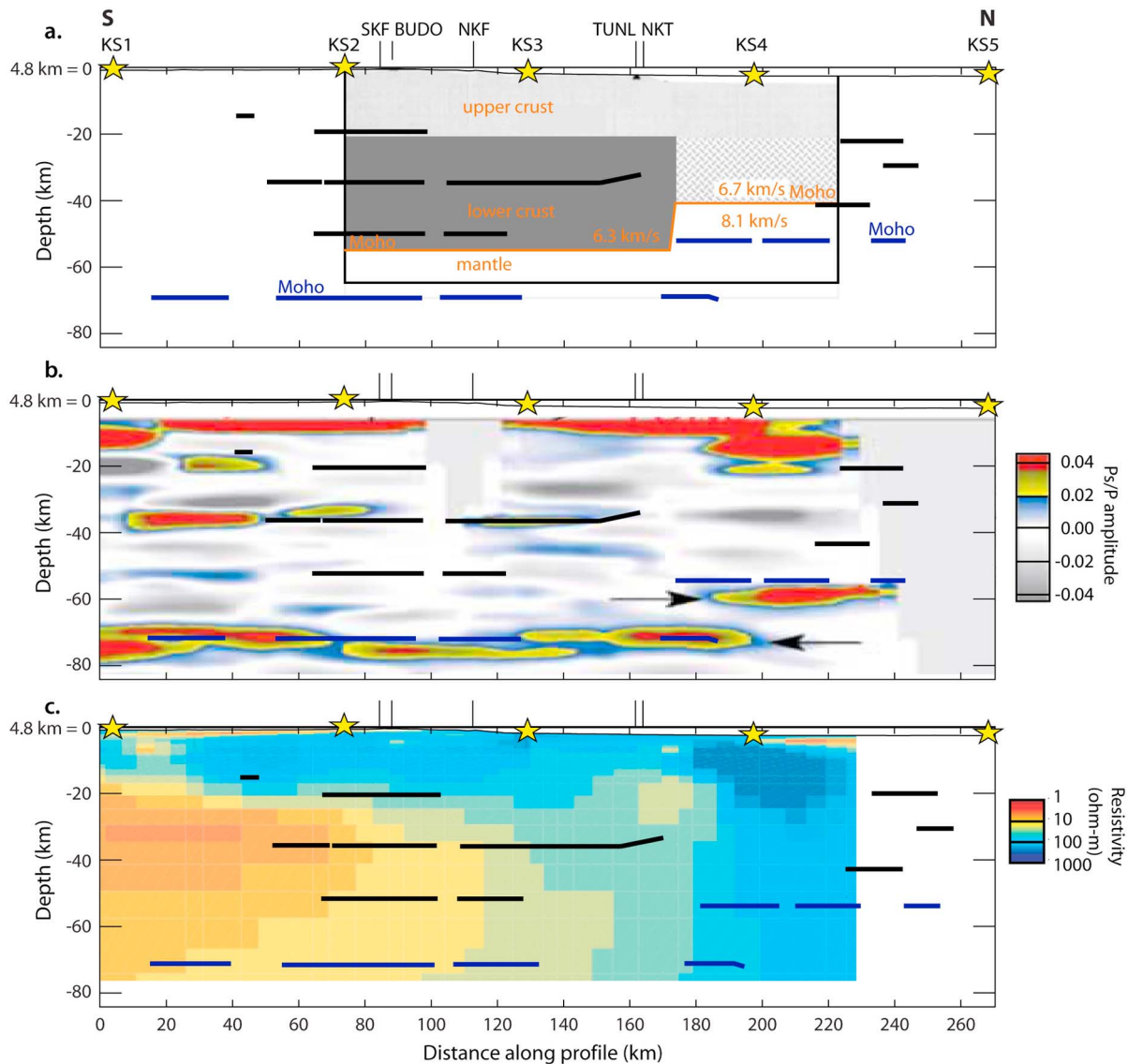


**Figure 12.** Moho (blue lines) and other reflectors (black lines) from our model superimposed on crustal models derived from (a) double-pulse teleseismic  $P$  wave arrivals (red line indicates Moho of *Zhu and HelMBERGER* [1998]), (b) teleseismic receiver functions along the Golmud-Lhasa highway [*Vergne et al.*, 2002], and (c) INDEPTH III magnetotelluric soundings along the Golmud-Lhasa highway [*Unsworth et al.*, 2004]. Large-shot locations are shown by yellow stars. BUDO and TUNL are PASSCAL broadband stations. SKF, South Kunlun Fault; NKF, North Kunlun Fault; NKT, North Kunlun Thrust. Vertical exaggeration is 1.

measurements were very close to the margin of the QB and may include velocity information from the EKM or other ranges bounding the basin. We conclude that the differences between the EKM and QB  $v$ - $z$  curves imply different crustal material in those two regions, as if they represent two separate terranes. The  $v$ - $z$  curves further suggest that the southernmost QB crust is generally the same as the central QB crust but with  $\sim 15$ – $20$  km of EKM injected beneath it.

[53] Figure 11c compares our  $v$ - $z$  curves for the SG, EKM, and QB with other terranes in Tibet from earlier phases of the INDEPTH project. To first order, the SG and EKM  $v$ - $z$  curves are very similar to the Lhasa and Qiangtang terrane curves, with thickened 70 km crust and velocities lower than the

average continental crust. There is strong evidence for partial melts or perhaps even channel flow in the middle to lower crust beneath south Tibet [*Nelson et al.*, 1996; *Klemperer*, 2006]. Seismic velocity is to some degree a proxy for crustal rheology. Between depths of 20–35 km and 50–70 km, the SG and EKM have even lower velocities than the Lhasa terrane. Hence, these are the most likely depth intervals for partial melts or channel flow beneath the SG and EKM.

#### 6.1.2. Broadband Seismic and MT Profiles

[54] *Zhu and HelMBERGER* [1998] and *Vergne et al.* [2002] both imaged Moho offsets of approximately the same magnitude as ours using lower-resolution teleseismic data (Figures 12a and 12b). *Zhu and HelMBERGER* [1998] show the

crust everywhere as 20 km thinner than we show, but their data do not constrain absolute thicknesses beneath the QB and EKM, only relative thicknesses. Vergne's receiver function image has remarkable similarities to our model, including intracrustal converters at 33 km (*Pi4P*). However, their velocity model includes a two-layer crust (upper felsic crust and lower mafic crust) beneath the Songpan-Ganzi terrane and Kunlun Mountains whereas we see a layer of low velocities in the middle crust between ~20–35 km depth that we infer to be a weak channel. Vergne *et al.*'s [2002] image also shows a strong Moho converter (suggestive of low lower-crustal velocities, as we observe) (note their profile follows the Golmud-Lhasa highway so is 200 km west of our model at the southern end), and even shows an overlap between the shallow QB Moho vertically above the deeper EKM Moho. Several hundred kilometers to the east, Shi *et al.* [2009] also show an overlapping Moho structure beneath the KQB with Kunlun and Qaidam Mohos at about the same depths as our profile.

[55] The INDEPTH III MT profile (Figure 12c) follows the Lhasa to Golmud highway into the southern part of the Qaidam Basin and contains a highly conductive middle-crustal layer at about 20 km (same depth as our *Pi2P* reflector) beneath the SG [Unsworth *et al.*, 2004]. The highly conductive layer is located at the same depths as a zone of low velocity from 20 to 35 km depth in our models of the SG and EKM and may represent a partial melt layer in the middle crust [Unsworth *et al.*, 2004]. Note that the inherent lack of vertical resolution in the MT method makes it impractical to distinguish a very thick layer of moderate conductivity (as shown) from multiple thinner layers of higher conductivity coincident with our middle- and lower-crustal layers of reduced velocity.

## 6.2. Origin of the Crustal Thickness Change in South Qaidam

[56] We compare our velocity structure to three families of models that attempt to account for the crustal thickening from QB to EKM: (1) crustal-penetrating NKF (Kunlun suture) (Figure 4a), (2) Asian lower-crustal subduction with the mantle suture beneath the NKF (Figures 4b and 4c), and (3) our new model, injection of Tibetan crust beneath Qaidam by crustal flow or lower-crustal underthrusting (Figure 13).

[57] Surface geologic mapping shows both south and north directed thrust faults in the East Kunlun Mountains [e.g., Yin *et al.*, 2007; Wu *et al.*, 2009]. As discussed in section 2.2, previous studies have postulated both major north directed and south directed thrust faults at the KQB. We incorporate a north directed NKT in our preferred model to explain the elevated topography to the south and the abrupt topographic front. There are middle-crustal reflectors at 20 km and 35 km in the south that may be décollement horizons (Figure 13a). While some geologic investigations have found no evidence of north directed faulting [Yin *et al.*, 2007], others have observed geomorphic features such as the distribution of lacustrine and playa depocenters along the KQB in the modern basin that support north vergent thrusts (B. Ritts, personal communication, 2010). However, our data do not rule out south directed thrusts, so Figure 13b offers an alternative incorporating south directed thrusts at the KQB.

### 6.2.1. Crustal-Penetrating NKF

[58] In this conceptual model, the Mesozoic Kunlun suture penetrates the entire crust, bringing thinner KQ crust in contact with thicker SG crust, and has been reactivated as a modern strike-slip fault that also cuts the entire crust [e.g., Tapponnier *et al.*, 2001; Chung *et al.*, 2005; Li *et al.*, 2011]. Studies of the Kokoxili earthquake (section 2.4) suggest the NKF has an 80° southward dip down to about 20 km [Lin *et al.*, 2003; King *et al.*, 2005]. Our new location of the Moho offset 100 km north of the NKF rules out the NKF as the cause of the Moho offset. If the NKF is a near-vertical fault to the Moho, it does not juxtapose terranes with different velocity structure, nor does it resolvably offset the Moho (Figure 8c).

### 6.2.2. Asian Lower-Crustal Subduction Beneath the NKF

[59] In this conceptual model, the crustal thickening from QB to SG is caused by subduction of the KQ crust and upper mantle beneath the SG crust, continuing at least to the Neogene [e.g., Meyer *et al.*, 1998; Yin *et al.*, 2008b]. The thicker SG crust is thrust over the thinner KQ terrane with the “mantle suture” (juxtaposition of distinct crustal terranes at the Moho) defining the location of the Moho offset. This model cannot simply be reconciled with the subhorizontal reflectors (*PmP*) at 52 km and 70 km beneath the southern portion of the QB between 166 and 215 km. A south vergent subduction system with dip comparable to that of the Himalayan intracontinental subduction zone (4°–11°) [Leech *et al.*, 2005] does not explain the overlapping *PmP* reflectors from 175 to 190 km, nor the near-vertical 15 km boundary between crustal and mantle material at 215 km. Suggestions that the Moho offset could potentially have been created by an older, now abandoned subduction system [e.g., Tapponnier *et al.*, 2001] meet the same geometric objections as the model of ongoing Asian subduction [e.g., Yin *et al.*, 2008b].

[60] A wedge model that incorporates subduction of Qaidam lower crust beneath and overthrusting of Qaidam upper crust above a “wedge” of SG material (Figure 4c) [e.g., Yin *et al.*, 2008b] seems implausible along our profile owing to the reflector geometries as well as the fact that the SG and KM crust has lower velocities and hence is likely weaker than the Qaidam crust. A Qaidam wedge around which SG material is moving or flowing (Figure 13) seems more plausible than a SG crustal wedge around which Qaidam crust is flowing (Figure 4c).

[61] Models incorporating deeper Asian subduction [Kind *et al.*, 2002; Zhao *et al.*, 2010] with a boundary dipping <10°S at ~100 km depth beneath the NKF offer no explanation for the observed Moho offset (Figure 4a) and cannot be tested by our active source experiment.

### 6.2.3. Injection of Tibetan Crust Beneath Qaidam Basin

[62] Having ruled out published conceptual models explaining the jump in crustal thickness with a crustal-scale NKF or south directed subduction, we suggest that the crustal thickness change is caused by the northward injection of SG and EKM lower crust beneath the QB (Figure 13). Our observations show that the transition from thicker to thinner crust is located 100 km north of the NKF and 45 km north of the NKT. Furthermore, our observations require a double Moho structure with crustal velocity material between the Qaidam

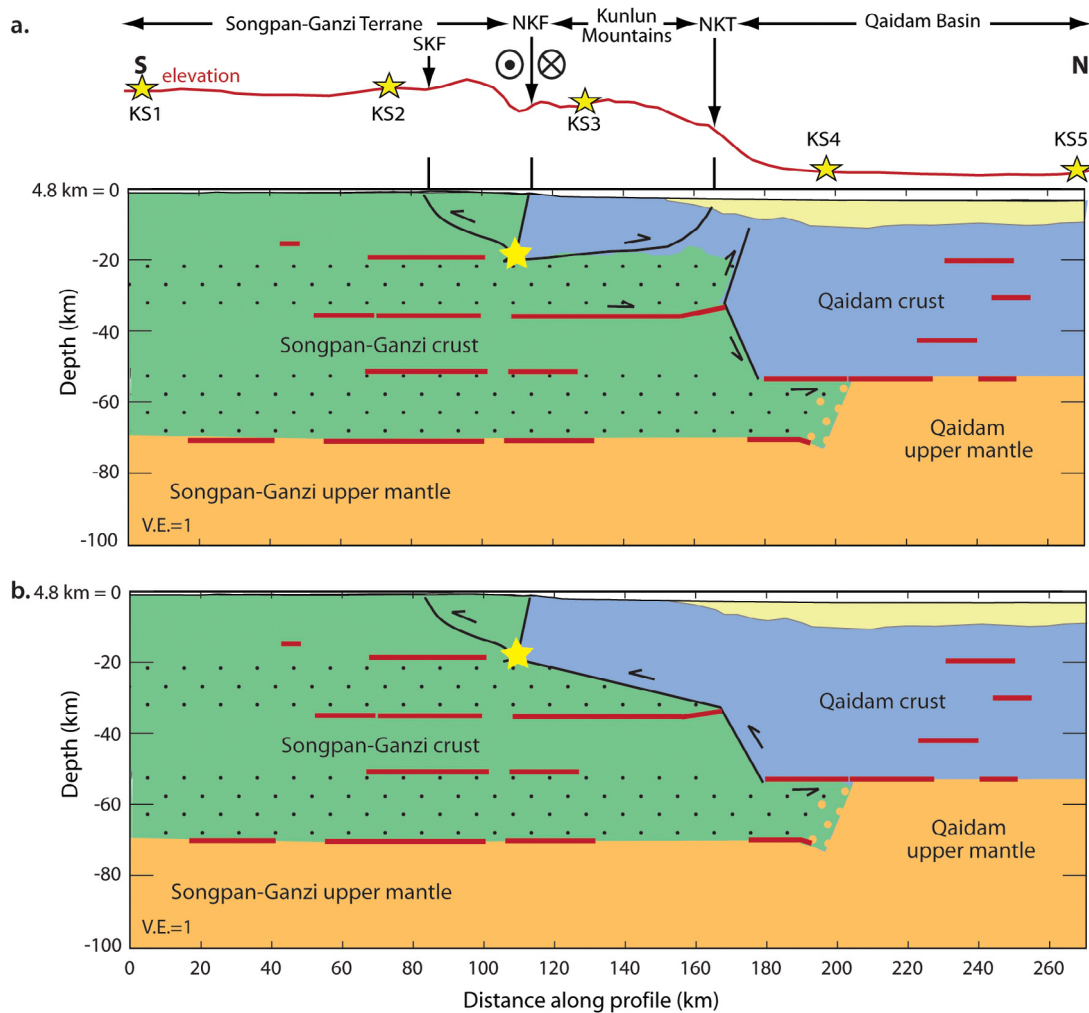


**Figure 13.** New tectonic models. Moho offset is the northern extent of lower-crustal material injected beneath Qaidam between ~190 and 205 km (mixed green and beige pattern). Black dots indicate regions of lowest velocity (compared to global average at that depth) that are the most likely zones of ductile flow containing some partial melt. Average elevation curve and fault abbreviations are as in Figure 8a. Red lines show reflectors and Moho structure from our seismic data. Yellow star indicates the 2001 Kokoxili earthquake hypocentral depth. (a) Preferred model. (b) Alternate model, also consistent with our velocity model, to illustrate that our data does not constrain the vergence of middle to upper crustal thrusts beneath the Kunlun Mountains.

Moho at 52 km and the deeper 70 km Moho near the location of that transition. We conclude that these observations are caused by SG and EKM lower crust thrusting or flowing beneath Qaidam crust.

[63] The depth intervals beneath the SG and EKM most likely to contain partial melts or flowing material are between 20–35 km and 50–70 km (Figure 13), if we use seismic velocity as a proxy for crustal rheology (section 6.1.1; see Figure 11). The 50 km *Pi6P* reflector beneath the SG and EKM corresponds to the top of a region of lower velocities from 50 to 70 km (Figure 11c), which may be the top of a lower-crustal flow channel. On the basis of its depth, this reflector may also be a relict shallower Moho with lower-crustal material thrusting or flowing beneath it.

[64] The crustal thickening above a northward moving channel (as well as associated with transpression across the

NKF) would further explain the elevated topography of the Kunlun range front and north vergent thrusts above and north of the channel front. *Clark and Royden* [2000] describe how crustal channel flow with different middle-crustal viscosities could explain differing topographic slopes at the eastern and northern margins of Tibet. In their model, the steep topographic front between the EKM and QB would imply a relatively high-viscosity channel, hence a slow flux within it. The injection of weak Tibetan crust beneath stronger QB crust may be a mechanism by which the EKM are actively growing northward into the QB. Other numerical models of channel flow [e.g., *Rey et al.*, 2010, Figure 2] yield crustal-scale geometries and transport length scales strikingly similar to our preferred model (Figure 13a) in which an underthrusting flow channel only propagates a few tens of km into the foreland of the orogen.

[65] About 350 km east of our profile, based on the presence of SmS reflections and on the high amplitude of PmP reflections along the Gonghe-Yushu profile, *Galvé et al.* [2002] conclude that there is no partial melt in the deep crust in NE Tibet (Figure 1). However, our velocity comparison suggests that SG crust is only slightly higher seismic velocity than Lhasa and Qiangtang crust, both strongly implicated to include partial melts, so that we should not exclude the possibility of limited partial melting. We might expect more partial melting on our INDEPTH profile at 95°E than on the Gonghe-Yushu profile that crosses the SG terrane between 97° and 99°E, because mid-Miocene to Quaternary volcanics scattered across the SG terrane die out east of 92°E [*Chung et al.*, 2005]. These volcanics include volumetrically minor leucogranites (crustal melts) but are dominantly shoshonitic melts from the lithospheric mantle [*Chung et al.*, 2005], perhaps arising in a mantle wedge above the deeper Asian subduction proposed by *Kind et al.* [2002] (Figure 4a).

[66] *Yin et al.* [2008b] propose using stratigraphic relationships to test whether lower-crustal flow is thickening the crust in south Qaidam. If lower-crustal channel flow uplifts the surface more slowly than the sedimentation rate, the basin margins should migrate away from the basin center resulting in transgressional stratigraphic relationships [*Yin et al.*, 2008b, Figure 19b]. The seismic reflection interpretations of *Yin et al.* [2008b, Figure 9] for central Qaidam northwest of the INDEPTH IV profile show exactly this relationship: the Quaternary sediments are transgressional and onlap the range front in south Qaidam. Our proposed 18 km thick channel yields a roughly 2 km uplift at Golmud if Airy isostasy applies, and crudely, because the Plio-Quaternary reaches 2 km thickness within 50 km of the range front [*Yin et al.*, 2008b, Figure 12], this amount of recent uplift could be hidden beneath these sediments. Of course, the uplift would taper over a much broader region if we allow for the strength of the Qaidam crust. Indeed, our proposed channel flow would lead to the northward tilting or warping of the southern Qaidam margin observed by *Yin et al.* [2008b] for the time periods 65–24 and 10–2 Ma. The second tilting event at 10 Ma may coincide with the beginning of northward injection or flow of lower-crustal material beneath south Qaidam.

## 7. Conclusions

[67] Our seismic velocity models add significant new details to our understanding of the boundary between the Qaidam Basin and SG terrane. Our velocity models from tomographic inversion of *Pg* and ray tracing of deeper reflections delineate distinct velocity versus depth curves beneath the SG, EKM, and QB. These models show an 8–14 km thick SG flysch with velocities of 4.2–5.9 km/s and a 4–6 km thick sedimentary Qaidam Basin. Relatively high near-surface velocities (greater than 5 km/s) are seen in the EKM along with a region of elevated velocity down to 20 km depth, likely caused by the Kunlun batholith and metamorphic rocks beneath the EKM. Shallow low-velocity anomalies down to 1–2 km exist at the surface locations of the SKF, NKF, and NKT.

[68] We confirm previous reports of a major change in crustal thickness between the EKM and the QB, but image its structure in detail and locate the abrupt 18 km change 100 km

north of the NKF (Kunlun suture). Immediately south of the step, we see clear evidence for crustal seismic velocities beneath the strong 52 km reflector that continues north as the Moho to the QB, implying a “double Moho” over a north-south extent of ~40 km. Gravity modeling confirms the existence of the Moho step and crustal densities beneath the Qaidam Basin Moho reflector. We infer the “double Moho” implies injection of SG or EKM material northward beneath the QB.

[69] The newly detailed geometry of the Moho step and the similarity of the SG velocity profiles to the Lhasa and Qiangtang velocity profiles support the existence of a middle-to lower-crustal flow channel within the 70 km thick SG crust as inferred for more southerly Tibetan terranes [e.g., *Klemperer*, 2006], though here beneath the SG and EKM with lateral transport of only a few tens of kilometers. Flow and pure shear thickening of Tibet creates the 70 km thickened crust, and the NKT uplifts the East Kunlun Mountains above the thickened crust. The Tibetan Plateau is growing northward as weak Tibetan crust is injected beneath stronger northern terranes.

## Appendix A

[70] Figure A1 shows the five large shot gathers displayed in reduced travel time. These gathers are identical to those in Figure 5, without the highlighted model refraction/reflection phases. Figure A2 shows the signals for earthquakes EQ4 and EQ13, recorded at 24 broadband phases. These records are identical to those in Figure 7, without the highlighted *PmP* and *Pn* phases.

## Appendix B

[71] A checkerboard test (Figures B1a and B1b) shows the regions in which our shallow tomography method can resolve velocity anomalies. We inverted a synthetic data set created by forward modeling a checkerboard of larger velocity anomalies ( $\pm 0.3$  km/s) than typical in our final model (Figure 8b) varying on shorter length scales (5 km horizontally and 3 km vertically) than interpreted in our final model, using the same shot and receiver geometry as in the actual experiment. Figure B1a shows the uniform grid of rectangular anomalies (5 km horizontally and 3 km vertically,  $\pm 0.3$  km/s) used in the initial checkerboard. Figure B1b shows the anomalies recovered by our tomographic modeling. The anomalies were recovered down to 9–12 km between 25 and 190 km. The Qaidam Basin is only resolved in the upper 3 km, except near the locations of shots KS4 and KS5 at 198 and 270 km. However, our ray trace modeling guided by prior knowledge of the basin geometry from hydrocarbon exploration provides additional constraints.

[72] Because our checkerboard test uses a coarser grid spacing and simpler starting model than the tomographic modeling used to create our final velocity model (Figure 8b), we also show the final velocity model derived from tomographic modeling using a 1-D (laterally uniform) starting model and the 5 km  $\times$  3 km grid (Figure B1c). Even though this grid is sparser than our previous grid between 60 and 180 km, the tomographic modeling still finds low-velocity anomalies at the SKF and NKF (shown by A and B in Figure B1c), a low-velocity zone beneath the SKF (LV in

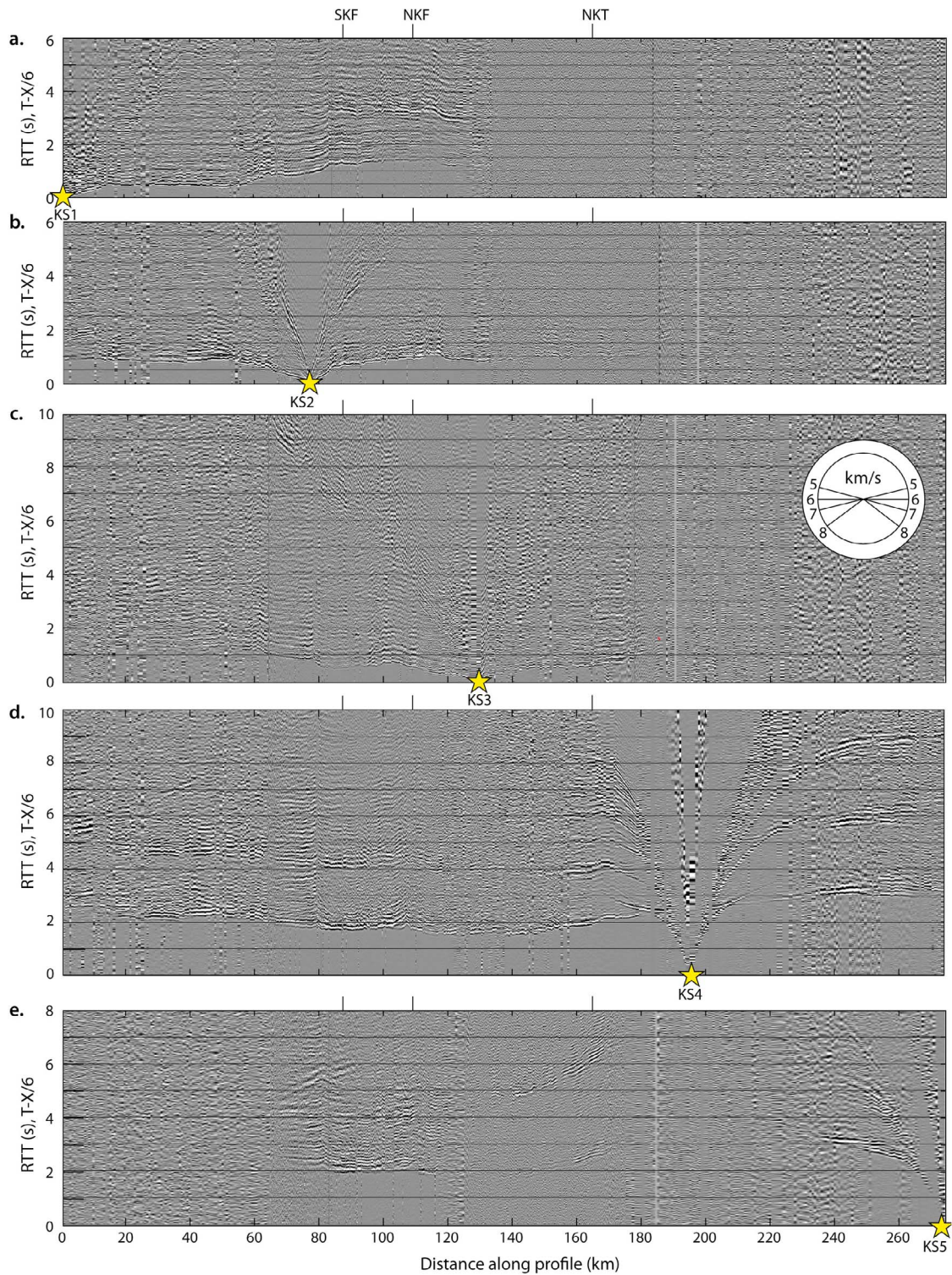


**Figure A1.** Large shot gathers displayed in reduced traveltime (RTT) for (a) KS1, (b) KS2, (c) KS3, (d) KS4, and (e) KS5. Velocity wheel in the KS3 gather in Figure A1c shows slopes of arrivals of velocities from 5 to 8 km/s. SKF, South Kunlun Fault; NKF, North Kunlun Fault; NKT, North Kunlun Thrust. Identical to Figure 5, but with no interpretation superimposed.

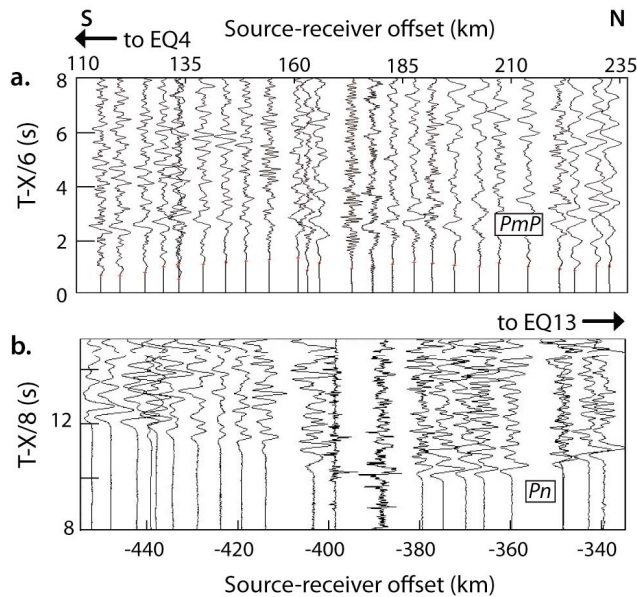


**Figure A2.** Earthquake records for (a) EQ4 and (b) EQ13 recorded on 20–25 broadband stations. Trace locations are displayed relative to the true earthquake–receiver offset. Identical to Figure 7, but with no interpretation superimposed. The x axes correspond to 60–185 km distance along the INDEPTH IV profile.

Figures 8b and B1c), a high-velocity zone beneath the NKF (HV in Figures 8b and B1c), and low velocities at the surface of the Qaidam Basin near shot points KS4 and KS5 at 200 and 268 km (E in Figure B1c). This model combined with the checkerboard test suggests that these features and rapid velocity fluctuations are well mapped by our data. At greater depths, and where there were no small shots in the Qaidam Basin, only smaller-magnitude and more gradational (longer-wavelength) velocity changes can be recovered.

[73] A model recovery test (Figure B2a) provides additional corroboration of the quality of our upper crustal model. We inverted the synthetic data set created by forward modeling ray propagation through our final upper crustal tomogram (Figure 8b), using the same shot and receiver geometry as in the actual experiment. The similarity of Figures 8b and B2a, with most deviations less than 0.15 km/s (Figure B2b), shows that the features of the shallow velocity model that we interpret in this paper can be recovered to a depth of about 10 km subsurface. The full crustal model is additionally constrained by later-arriving reflected phases.

### Appendix C

[74] In order to further test the sensitivity of the lateral position of the change in crustal thickness, we computed gravities and traveltimes for structural models with the crustal thickness change relocated 10 km south and 10 km north of our preferred velocity model. The results of these tests are shown in Figure C1. The location of the Moho step cannot be moved north or south more than 10 km, unless the shallow densities, converted from the shallow velocities that are the best constrained part of the velocity model, are also changed.

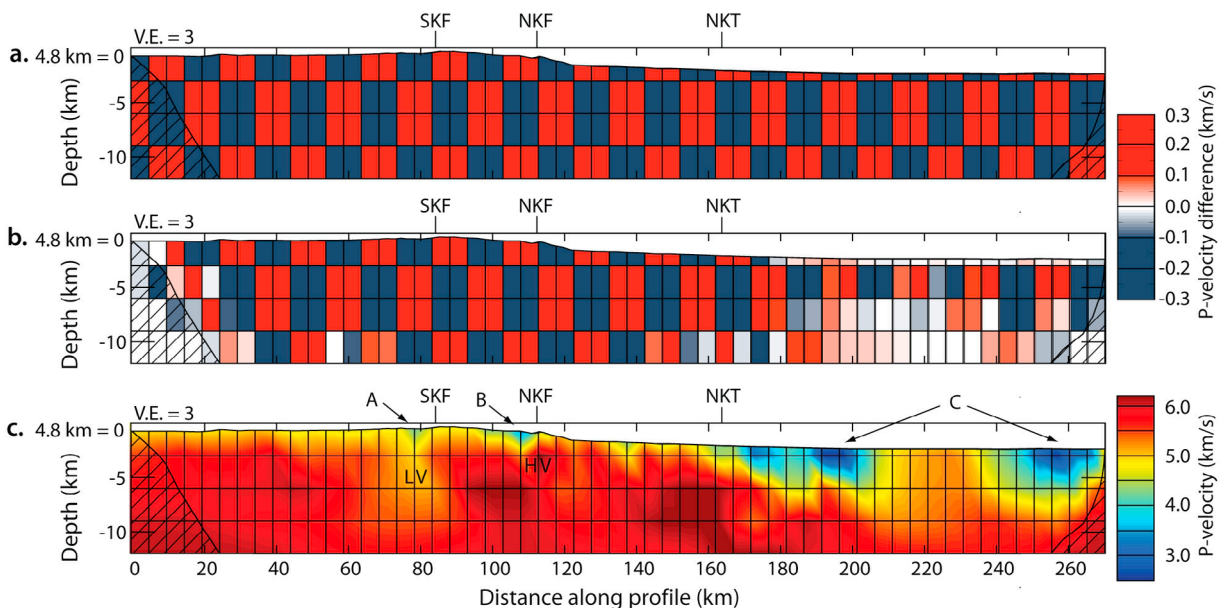


**Figure B1.** (a) Initial checkerboard of  $\pm 0.3$  km/s  $P$  velocity anomalies with uniform rectangular grid spacing of 5 km horizontal by 3 km vertical. (b) Final recovered  $P$  velocity anomalies for the checkerboard test are shown by the blue (negative) to red (positive) color fill. (c) Velocity model from the tomographic inversion of INDEPTH data using the same grid spacing as in Figures B1a and B1b, and a 1-D (laterally uniform) starting velocity model. The letters A and B represent unusually low velocities near the surface traces of the South Kunlun Fault (SKF) and North Kunlun Fault (NKF). LV, low-velocity region; HV, high-velocity region (corresponding to LV and HV in Figure 8b). The letter C represents low near-surface velocities in the Qaidam Basin.

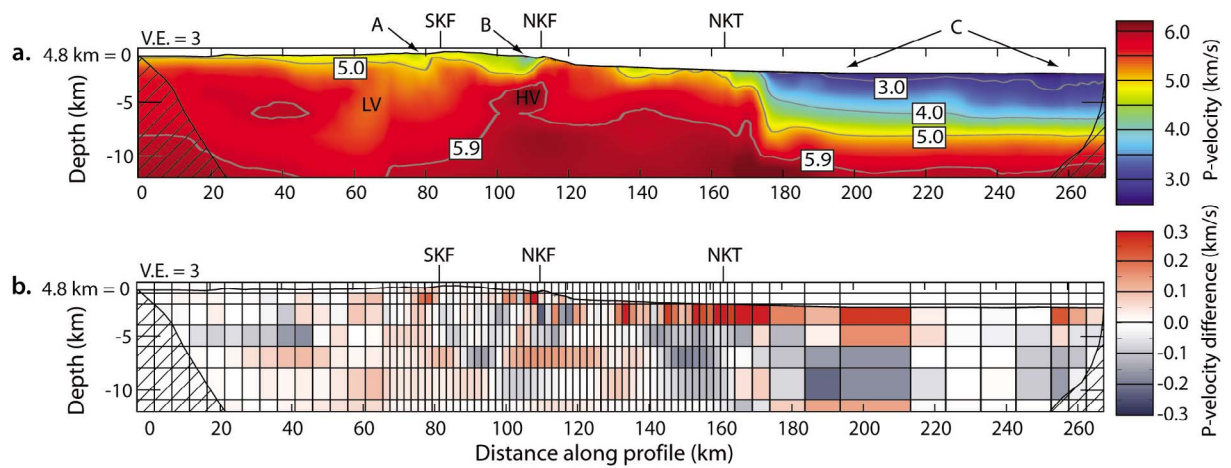


**Figure B2.** (a) Final recovered shallow velocity model from the model recovery test. The letters A and B represent unusually low velocities near the surface traces of the South Kunlun Fault (SKF) and North Kunlun Fault (NKF). LV, low-velocity region; HV, high-velocity region (corresponding to LV and HV in Figure 8b). The letter C represents low near-surface velocities in the Qaidam Basin. (b) Difference between initial tomographic velocity model (Figure 8b) and recovered velocity model from the model recovery test.

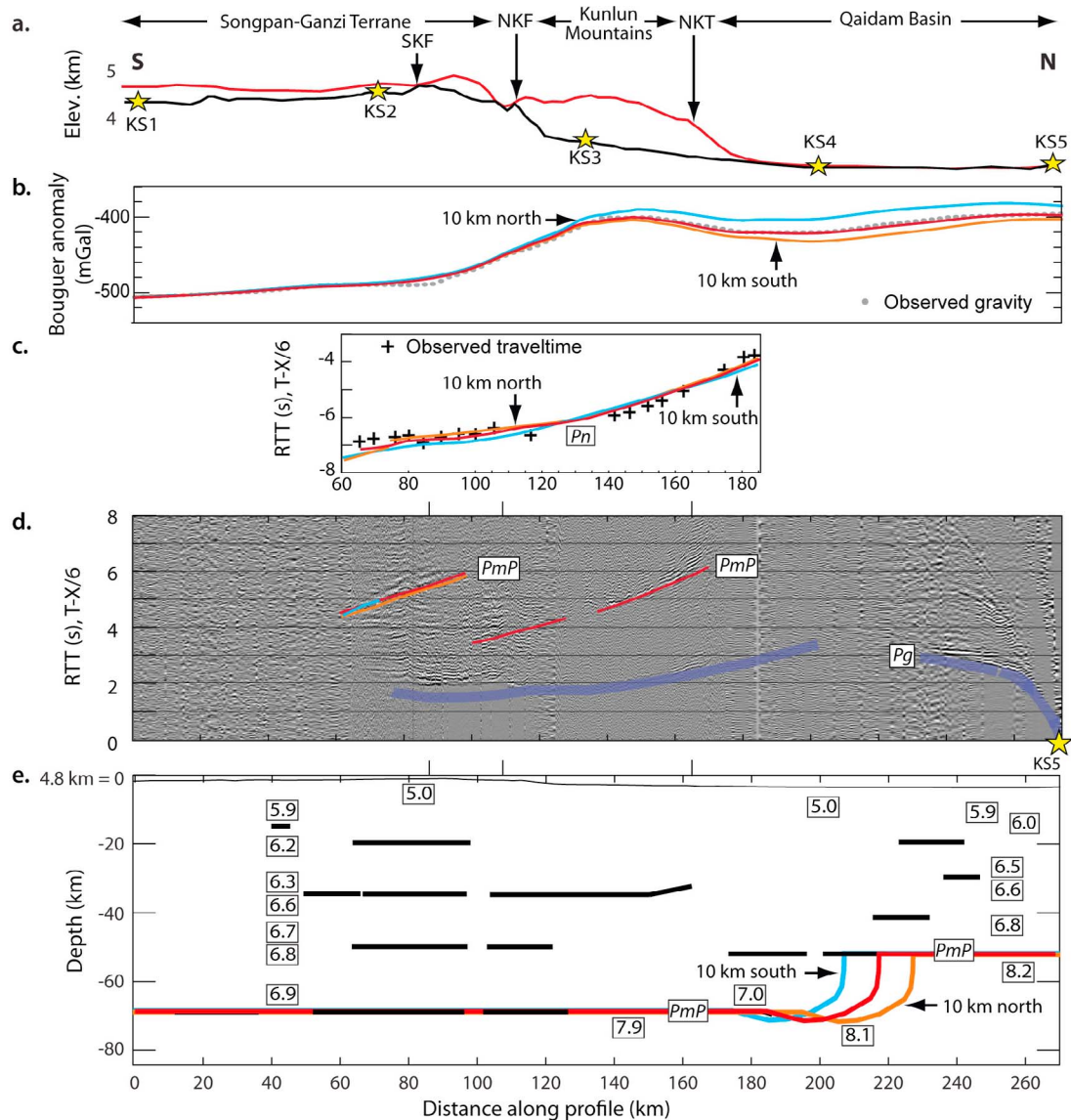


**Figure C1.** Testing the lateral position of the change in crustal thickness. Moho geometries, modeled traveltimes, and modeled gravity curves are shown for the preferred deep Moho geometry (red curve; see Figure 8c), the location of crustal thickness change moved 10 km south (blue curve), and the location of crustal thickness change moved 10 km north (orange curve). (a) Elevation along the INDEPTH IV profile (Figure 8a). (b) Bouguer anomaly data (gray dots) (Figure 10b) plotted with calculated gravity curves for the three Moho scenarios. (c) EQ13 mantle refraction ( $P_n$ )–modeled traveltime curves for the three Moho scenarios overlain on the traveltime picks for 24 seismic stations (see Figure 6b). (d) Large-shot gather KS5 (Figure 5e). Blue curve shows model-calculated traveltimes from first-arrival tomography. Red curve is the reflection model-calculated traveltime curve using the preferred model. The other traveltime curves correspond to the two alternate Moho scenarios. Curves are only displayed in the vicinity of actual data picks. (e) Composite shallow and deep crustal velocity model from ray tracing the INDEPTH IV controlled-source profile (Figure 8c) with the three Moho structures being tested. Major reflectors shown as black lines. No vertical exaggeration.

[75] **Acknowledgments.** We thank PASSCAL, SEIS-UK, and GIPP-GFZ Potsdam for the use of instruments, and we thank the entire INDEPTH field team. All our reflection/refraction data and associated metadata are freely available from IRIS-DMC at <http://www.iris.edu/data/>. INDEPTH activities are funded by NSF-EAR-CD-0409939, Deutsche Forschungsgemeinschaft, GFZ Potsdam, and CGS-1212010511809 in China. We thank Walter Mooney and Jonathan Glen at the USGS for their suggestions regarding the seismic and gravity data, respectively. We thank Bradley Ritts, An Yin, and two anonymous reviewers for their comments on the manuscript. An NSF graduate fellowship and a Stanford McGee Grant supported M. S. Karplus. ProMAX reflection processing software was provided through a Landmark academic grant.

## References

- Bally, A. W., I.-M. Chou, R. Clayton, H. P. Eugster, S. Kidwell, L. D. Meckel, R. T. Ryder, A. B. Watts, and A. A. Wilson (1986), Notes on sedimentary basins in China—Report of the American Sedimentary Basins Delegation to the People's Republic of China, *U.S. Geol. Surv. Open File Rep.*, 86-327, 1–108.
- Beaumont, C., R. A. Jamieson, M. H. Nguyen, and S. Medvedev (2004), Crustal channel flows: 1. Numerical models with applications to the tectonics of the Himalayan-Tibetan orogen, *J. Geophys. Res.*, *109*, B06406, doi:10.1029/2003JB002809.
- Bian, Q., et al. (2004), Age, geochemistry and tectonic setting of Buqingshan ophiolites, North Qinghai-Tibet Plateau, China, *J. Asian Earth Sci.*, *23*, 577–596, doi:10.1016/j.jseas.2003.09.003.
- Brocher, T. M. (2005), Empirical relations between elastic wavespeeds and density in the Earth's crust, *Bull. Seismol. Soc. Am.*, *95*, 2081–2092, doi:10.1785/0120050077.
- Burchfiel, B., Q. Deng, P. Molnar, L. Royden, Y. Wang, P. Zhang, and W. Zhang (1989), Intracrustal detachment within zones of continental deformation, *Geology*, *17*, 748–752, doi:10.1130/0091-7613(1989)017<0448:IDWZOC>2.3.CO;2.
- Burchfiel, B., Z. Chen, Y. Liu, and L. Royden (1995), Tectonics of the Longmen Shan and adjacent regions, central China, *Int. Geol. Rev.*, *37*, 661–735, doi:10.1080/00206819509465424.
- Cervený, V., I. Molotkov, and I. Psencik (1977), *Ray Method in Seismology*, Charles Univ., Prague.
- Chen, W., C. Chen, and J. Nabelek (1999), Present-day deformation of the Qaidam Basin with implications for intra-continental tectonics, *Tectonophysics*, *305*, 165–181, doi:10.1016/S0040-1951(99)00006-2.
- Christensen, N. I., and W. Mooney (1995), Seismic velocity structure and composition of the continental crust: A global view, *J. Geophys. Res.*, *100*, 9761–9788, doi:10.1029/95JB00259.
- Chung, S., M. Chu, Y. Zhang, Y. Xie, C. Lo, T. Lee, C. Lan, X. Li, Q. Zhang, and Y. Wang (2005), Tibetan tectonic evolution inferred from spatial and temporal variations in post-collisional magmatism, *Earth Sci. Rev.*, *68*, 173–196, doi:10.1016/j.earscirev.2004.05.001.
- Clark, M., and L. Royden (2000), Topographic ooze: Building the eastern margin of Tibet by lower crustal flow, *Geology*, *28*, 703–706, doi:10.1130/0091-7613(2000)28<703:TOBTEM>2.0.CO;2.
- Clark, M., K. Farley, D. Zheng, Z. Wang, and A. R. Duvall (2010), Early Cenozoic faulting of the northern Tibetan Plateau margin from apatite (U–Th)/He ages, *Earth Planet. Sci. Lett.*, *296*, 78–88, doi:10.1016/j.epsl.2010.04.051.
- Cowgill, E., A. Yin, T. M. Harrison, and W. Xiao-Feng (2003), Reconstruction of the Altyn Tagh Fault based on U–Pb geochronology: Role of back thrusts, mantle sutures, and heterogeneous crustal strength in forming the Tibetan Plateau, *J. Geophys. Res.*, *108*(B7), 2346, doi:10.1029/2002JB002080.
- DeCelles, P. G., D. M. Robinson, and G. Zandt (2002), Implications of shortening in the Himalayan fold-thrust belt for uplift of the Tibetan Plateau, *Tectonics*, *21*(6), 1062, doi:10.1029/2001TC001322.
- England, P., and G. Houseman (1986), Finite strain calculations of continental deformation: 2. Comparison with the India-Asia collision zone, *J. Geophys. Res.*, *91*, 3664–3676, doi:10.1029/JB091iB03p03664.
- Fu, B., and Y. Awata (2007), Displacement and timing of left-lateral faulting in the Kunlun Fault Zone, northern Tibet, inferred from geologic and geomorphic features, *J. Asian Earth Sci.*, *29*, 253–265, doi:10.1016/j.jseas.2006.03.004.
- Fu, B., Y. Awata, J. Du, Y. Ninomiya, and W. He (2005), Complex geometry and segmentation of the surface rupture associated with the 14 November 2001 great Kunlun earthquake, northern Tibet, China, *Tectonophysics*, *407*, 43–63, doi:10.1016/j.tecto.2005.07.002.
- Galvé, A., A. Hirn, M. Jiang, J. Gallart, B. de Voogd, J. Lépine, J. Diaz, Y. Wang, and H. Qian (2002), Modes of raising northeastern Tibet probed by explosion seismology, *Earth Planet. Sci. Lett.*, *203*, 35–43, doi:10.1016/S0012-821X(02)00863-4.
- Guillot, S., E. Garzanti, D. Baratoux, D. Marquer, G. Mahéo, and J. de Sigoyer (2003), Reconstructing the total shortening history of the NW Himalaya, *Geochim. Geophys. Geosyst.*, *4*(7), 1064, doi:10.1029/2002GC000484.
- Harkins, N., E. Kirby, X. Shi, E. Wang, D. Burbank, and F. Chun (2010), Millennial slip rates along the eastern Kunlun Fault: Implications for the dynamics of intracontinental deformation in Asia, *Lithosphere*, *2*, 247–266, doi:10.1130/L85.1.
- Jiang, M., A. Galvé, A. Hirn, B. de Voogd, M. Laigle, H. Su, J. Diaz, J. Lépine, and Y. Wang (2006), Crustal thickening and variations in architecture from the Qaidam Basin to the Qang Tang (north central Tibetan Plateau) from wide-angle reflection seismology, *Tectonophysics*, *412*, 121–140, doi:10.1016/j.tecto.2005.09.011.
- Jolivet, M., M. Brunel, D. Seward, Z. Xu, J. Yang, J. Malavieille, F. Roger, A. Leyreloup, N. Arnaud, and C. Wu (2003), Neogene extension and volcanism in the Kunlun Fault Zone, northern Tibet: New constraints on the age of the Kunlun Fault, *Tectonics*, *22*(5), 1052, doi:10.1029/2002TC001428.
- Kidd, W. S. F., and P. Molnar (1988), Quaternary and active faulting observed on the 1985 Academia Sinica–Royal Society Geotraverse of Tibet, *Philos. Trans. R. Soc. London A*, *327*, 337–363, doi:10.1098/rsta.1988.0133.
- Kind, R., et al. (2002), Seismic images of crust and upper mantle beneath Tibet: Evidence for Eurasian plate subduction, *Science*, *298*, 1219–1221, doi:10.1126/science.1078115.
- King, G., Y. Klinger, D. Bowman, and P. Tapponnier (2005), Slip-partitioned surface breaks for the Mw 7.8 2001 Kokoxili earthquake, China, *Bull. Seismol. Soc. Am.*, *95*, 731–738, doi:10.1785/0120040101.
- Klemperer, S. (2006), Crustal flow in Tibet: Geophysical evidence for the physical state of Tibetan lithosphere, and inferred patterns of active flow, *Geol. Soc. Spec. Publ.*, *268*, 39–70, doi:10.1144/GSL.SP.2006.268.01.03.
- Kosarev, G., R. Kind, S. V. Sobolev, X. Yuan, W. Hanka, and S. Oreshin (1999), Seismic evidence for a detached Indian lithospheric mantle beneath Tibet, *Science*, *283*, 1306–1309, doi:10.1126/science.283.5406.1306.
- Leech, M., S. Singh, A. Jain, S. Klemperer, and R. Manickavasagam (2005), The onset of India-Asia continental collision: Early, steep subduction required by the timing of UHP metamorphism in the western Himalaya, *Earth Planet. Sci. Lett.*, *234*, 83–97, doi:10.1016/j.epsl.2005.02.038.
- Li, Q., S. Peng, R. Gao, Y. Guan, and J. Fan (2004), Deep tectonic background of the 8.1 Ms earthquake in the East Kunlun (in Chinese with English abstract), *Acta Geosci. Sinica*, *25*, 11–16.
- Li, Y., Q. Wu, F. Zhang, Q. Feng, and R. Zhang (2011), Seismic anisotropy of the northeastern Tibetan Plateau from shear wave splitting analysis, *Earth Planet. Sci. Lett.*, *304*, 147–157, doi:10.1016/j.epsl.2011.01.026.
- Lin, A., M. Kikuchi, and B. Fu (2003), Rupture segmentation and process of the 2001 Mw 7.8 central Kunlun, China, earthquake, *Bull. Seismol. Soc. Am.*, *93*, 2477–2492, doi:10.1785/0120020179.
- Liu, M., W. Mooney, S. Li, N. Okaya, and S. Detweiler (2006), Crustal structure of the northeastern margin of the Tibetan plateau from the Songpan-Ganzi terrane in the Ordos Basin, *Tectonophysics*, *420*, 253–266, doi:10.1016/j.tecto.2006.01.025.
- Lutter, W., R. Nowack, and L. Braile (1990), Seismic imaging of upper crustal structure using traveltimes from the PASSCAL Ouachita experiment, *J. Geophys. Res.*, *95*, 4621–4631, doi:10.1029/JB095iB04p04621.
- Mechie, J., et al. (2007), Three-component seismic observations within the INDEPTH IV transect: NE Tibetan Plateau to Qaidam Basin, *Eos Trans. AGU*, *88*(52), Fall Meet. Suppl., Abstract T31B–0471.
- Meng, L., Y. Guan, L. Qi, and R. Gao (1995), Gravity field and deep crustal structure in Golmud-Ejin Qi geoscience transect and nearby area (in Chinese), *Chin. J. Geophys.*, *38*, 36–45.
- Meyer, B., P. Tapponnier, L. Bourjot, F. Métivier, Y. Gaudemer, G. Peltzer, G. Shummin, and C. Zhitai (1998), Crustal thickening in Gansu-Qinghai, lithospheric mantle subduction, and oblique, strike-slip controlled growth of the Tibet plateau, *Geophys. J. Int.*, *135*, 1–47, doi:10.1046/j.1365-246X.1998.00567.x.
- Mock, C., J. Cantagrel, and N. O. Arnaud (1999), An early unroofing in northeastern Tibet? Constraints from <sup>40</sup>Ar/<sup>39</sup>Ar thermochronology on granitoids from the eastern Kunlun range (Qinghai, NW China), *Earth Planet. Sci. Lett.*, *171*, 107–122, doi:10.1016/S0012-821X(99)00133-8.
- Nábelek, J., G. Hetényi, J. Vergne, S. Sapkota, B. Kafle, M. Jiang, H. Su, J. Chen, and B.-S. Huang (2009), Unraveling in the Himalaya-Tibet collision zone revealed by the Hi-CLIMB experiment, *Science*, *325*, 1371–1374, doi:10.1126/science.1167719.
- Nelson, K., W. Zhao, L. Brown, J. Kuo, J. Che, X. Liu, S. Klemperer, Y. Makovsky, R. Meissner, and J. Mechie (1996), Partially molten middle crust beneath southern Tibet: Synthesis of project INDEPTH results, *Science*, *274*, 1684–1688, doi:10.1126/science.274.5293.1684.

- Owens, T., and G. Zandt (1997), Implications of crustal property variations for models of Tibetan plateau evolution, *Nature*, **387**, 37–43, doi:10.1038/387037a0.
- Paige, C., and M. Saunders (1982), LSQR: An algorithm for sparse linear equations and sparse least squares, *Trans. Math. Software*, **8**, 43–71, doi:10.1145/355984.355989.
- Pan, G., J. Ding, D. Yao, and L. Wang (2004), *Geological Map of the Qinghai-Xizang (Tibet) Plateau and Adjacent Areas*, Chengdu Inst. of Geol. and Miner. Resour., Chengdu, China.
- Rey, P. F., C. Teyssier, and D. L. Whitney (2010), Limit of channel flow in orogenic plateaux, *Lithosphere*, **2**, 328–332, doi:10.1130/L114.1.
- Roger, F., N. Arnaud, S. Gilder, P. Tapponnier, M. Jolivet, M. Brunel, J. Malavieille, Z. Xu, and J. Yang (2003), Geochronological and geochemical constraints on Mesozoic suturing in east central Tibet, *Tectonics*, **22**(4), 1037, doi:10.1029/2002TC001466.
- Sengör, A. M. C., D. Altiner, A. Cin, T. Ustaömer, K. J. Hsü, A. M. C. Seng, D. Altiner, A. Cin, T. Ustaömer, and K. J. Hsü (1988), Origin and assembly of the Tethyside orogenic collage at the expense of Gondwana Land, *Spec. Publ. Geol. Soc. London*, **37**, 119–181, doi:10.1144/GSL.SP.1988.037.01.09.
- Shi, D., Y. Shen, W. Zhao, and A. Li (2009), Seismic evidence for a Moho offset and south directed thrust at the easternmost Qaidam-Kunlun boundary in the Northeast Tibetan plateau, *Earth Planet. Sci. Lett.*, **288**, 329–334, doi:10.1016/j.epsl.2009.09.036.
- Song, T., and X. Wang (1993), Structural styles and stratigraphic patterns of syndepositional faults in a contractional setting: Examples from Qaidam Basin, northwestern China, *AAPG Bull.*, **77**, 102–117.
- Tapponnier, P., and P. Molnar (1976), Slip-line field theory and large-scale continental tectonics, *Nature*, **264**, 319–324, doi:10.1038/264319a0.
- Tapponnier, P., Z. Xu, F. Roger, B. Meyer, N. Arnaud, G. Wittlinger, and Y. Jingsui (2001), Oblique stepwise rise and growth of the Tibet Plateau, *Science*, **294**, 1671–1677, doi:10.1126/science.105978.
- Unsworth, M., W. Wenbo, A. Jones, S. Li, P. Bedrosian, J. Booker, J. Sheng, D. Ming, and T. Handong (2004), Crustal and upper mantle structure of northern Tibet imaged with magnetotelluric data, *J. Geophys. Res.*, **109**, B02403, doi:10.1029/2002JB002305.
- Vergne, J., G. Wittlinger, Q. Hui, P. Tapponnier, G. Poupinet, J. Mei, G. Herquel, and A. Paul (2002), Seismic evidence for stepwise thickening of the crust across the NE Tibetan plateau, *Earth Planet. Sci. Lett.*, **203**, 25–33, doi:10.1016/S0012-821X(02)00853-1.
- Vidale, J. (1988), Finite-difference calculation of traveltimes, *Bull. Seismol. Soc. Am.*, **78**, 2062–2076.
- Wang, C., H. Lou, J. Yang, W. D. Mooney, Z. Ding, and Z. Yao (2009), Shallow seismic structure of Kunlun fault zone in northern Tibetan Plateau, China: Implications for the 2001 Ms 8.1 Kunlun earthquake, *Geophys. J. Int.*, **177**, 978–1000, doi:10.1111/j.1365-246X.2009.04049.x.
- Wang, Q., and M. P. Coward (1990), The Chaidam Basin (NW China): Formation and hydrocarbon potential, *J. Pet. Geol.*, **13**, 93–112, doi:10.1111/j.1747-5457.1990.tb00255.x.
- Wang, Q., et al. (2001), Present-day crustal deformation in China constrained by global positioning system measurements, *Science*, **294**, 574–577, doi:10.1126/science.1063647.
- Wei, S., et al. (2010), Regional earthquakes in northern Tibetan Plateau: Implications for lithospheric strength in Tibet, *Geophys. Res. Lett.*, **37**, L19307, doi:10.1029/2010GL044800.
- Weislogel, A. L. (2008), Tectonostratigraphic and geochronologic constraints on evolution of the northeast Paleotethys from the Songpan-Ganzi complex, central China, *Tectonophysics*, **451**, 331–345, doi:10.1016/j.tecto.2007.11.053.
- White, R., D. McKenzie, and R. O’Nions (1992), Oceanic crustal thickness from seismic measurements and rare earth element inversions, *J. Geophys. Res.*, **97**, 19,683–19,715, doi:10.1029/92JB01749.
- Wittlinger, G., et al. (1996), Seismic tomography of northern Tibet and Kunlun: Evidence for crustal blocks and mantle velocity contrasts, *Earth Planet. Sci. Lett.*, **139**, 263–279, doi:10.1016/0012-821X(95)00235-5.
- Wu, G., et al. (1991), *Yadong to Golmud Transect Qinghai-Tibet Plateau, China*, AGU, Washington, D. C.
- Wu, Z., P. Ye, P. Barosh, D. Hu, W. Zhao, and Z. Wu (2009), Late Oligocene-early Miocene thrusting in southern East Kunlun Mountains, northern Tibetan Plateau, *J. Earth Sci.*, **20**, 381–390, doi:10.1007/s12583-009-0031-2.
- Xia, W., N. Zhang, X. Yuan, L. Fan, and B. Zhang (2001), Cenozoic Qaidam Basin, China: A stronger tectonic inverted, extensional rifted basin, *AAPG Bull.*, **85**, 715–736.
- Yin, A. (2006), Cenozoic tectonic evolution of the Himalayan orogen as constrained by along-strike variation of structural geometry, exhumation history, and foreland sedimentation, *Earth Sci. Rev.*, **76**, 1–131, doi:10.1016/j.earscirev.2005.05.004.
- Yin, A., and T. M. Harrison (2000), Geologic evolution of the Himalayan-Tibetan orogen, *Annu. Rev. Earth Planet. Sci.*, **28**, 211–280, doi:10.1146/annurev.earth.28.1.211.
- Yin, A., and S. Nie (1993), An indentation model for the north and south China collision and the development of the Tan-Lu and Honam fault systems, eastern Asia, *Tectonics*, **12**, 801–813, doi:10.1029/93TC00313.
- Yin, A., Y. Dang, M. Zhang, M. W. McRivette, W. P. Burgess, and X. Chen (2007), Cenozoic tectonic evolution of Qaidam Basin and its surrounding regions (part 2): Wedge tectonics in southern Qaidam Basin and the Eastern Kunlun Range, *Spec. Pap. Geol. Soc. Am.*, **433**, 369–390, doi:10.1130/2007.2433(18).
- Yin, A., Y. Dang, L. Wang, W. Jiang, S. Zhou, X. Chen, G. E. Gehrels, and M. W. McRivette (2008a), Cenozoic tectonic evolution of Qaidam Basin and its surrounding regions (part 1): The southern Qilian Shan-Nan Shan thrust belt and northern Qaidam Basin, *Geol. Soc. Am. Bull.*, **120**, 813–846, doi:10.1130/B26180.1.
- Yin, A., Y. Dang, M. Zhang, X. Chen, and M. W. McRivette (2008b), Cenozoic tectonic evolution of Qaidam Basin and its surrounding regions (part 3): Structural geology, sedimentation, and regional tectonic reconstruction, *Geol. Soc. Am. Bull.*, **120**, 847–876, doi:10.1130/B26232.1.
- Yuan, C., M. Zhou, M. Sun, Y. Zhao, S. Wilde, X. Long, and D. Yan (2010), Triassic granitoids in the eastern Songpan-Ganzi Fold Belt, SW China: Magmatic response to geodynamics of the deep lithosphere, *Earth Planet. Sci. Lett.*, **290**, 481–492, doi:10.1016/j.epsl.2010.01.005.
- Zelt, C. A., and R. B. Smith (1992), Seismic traveltime inversion for 2-D crustal velocity structure, *Geophys. J. Int.*, **108**, 16–34, doi:10.1111/j.1365-246X.1992.tb00836.x.
- Zhang, P.-Z., et al. (2004), Continuous deformation of the Tibetan Plateau from global positioning system data, *Geology*, **32**, 809–812, doi:10.1130/G20554.1.
- Zhang, Z., S. Klemperer, Z. Bai, Y. Chen, and J. Teng (2011), Crustal structure of the Paleozoic Kunlun orogeny from an active-source seismic profile between Moba and Guide in east Tibet, China, *Gondwana Res.*, **19**, 994–1007, doi:10.1016/j.gr.2010.09.008.
- Zhao, W., and W. Morgan (1987), Injection of Indian crust into Tibetan lower crust: A two-dimensional finite element model study, *Tectonics*, **6**, 489–504, doi:10.1029/TC006i004p00489.
- Zhao, W., K. Nelson, J. Che, J. Quo, D. Lu, C. Wu, and X. Liu (1993), Deep seismic reflection evidence for continental underthrusting beneath southern Tibet, *Nature*, **366**, 557–559, doi:10.1038/366557a0.
- Zhao, W., et al. (2001), Crustal structure of central Tibet as derived from project INDEPTH wide-angle seismic data INDEPTH III N-S seismic profile, *Geophys. J. Int.*, **145**, 486–498, doi:10.1046/j.0956-540x.2001.01402.x.
- Zhao, J., W. Mooney, X. Zhang, Z. Li, Z. Jin, and N. Okaya (2006), Crustal structure across the Altyn Tagh Range at the northern margin of the Tibetan Plateau and tectonic implications, *Earth Planet. Sci. Lett.*, **241**, 804–814, doi:10.1016/j.epsl.2005.11.003.
- Zhao, W., L. Brown, Z. Wu, S. L. Klemperer, D. Shi, J. Mechie, H. Su, F. Tilmann, M. S. Karplus, and Y. Makovsky (2008), Seismology across the northeastern edge of the Tibetan Plateau, *Eos Trans. AGU*, **89**(48), 487–488, doi:10.1029/2008EO480002.
- Zhao, J., et al. (2010), The boundary between the Indian and Asian tectonic plates below Tibet, *Proc. Natl. Acad. Sci. U. S. A.*, **107**, 11,229–11,233, doi:10.1073/pnas.1001921107.
- Zhou, D., and S. Graham (1996), Songpan-Ganzi complex of west Qinling Shan as Triassic remnant ocean basin fill trapped during the Mesozoic tectonic amalgamation of China, in *Tectonic Evolution of Asia*, edited by A. Yin and T. M. Harrison, pp. 281–299, Cambridge Univ. Press, Cambridge, U. K.
- Zhou, J., F. Xu, T. Wang, A. Cao, and C. Yin (2006), Cenozoic deformation history of the Qaidam Basin, NW China: Results from cross-section restoration and implications for Qinghai-Tibet Plateau tectonics, *Earth Planet. Sci. Lett.*, **243**, 195–210, doi:10.1016/j.epsl.2005.11.033.
- Zhu, L., and D. Helmberger (1998), Moho offset across the northern margin of the Tibetan Plateau, *Science*, **281**, 1170–1172, doi:10.1126/science.281.5380.1170.

L. D. Brown and C. Chen, Department of Earth and Atmospheric Sciences, Cornell University, Snee Hall, Rm. 2116, Ithaca, NY 14853, USA.  
M. S. Karplus and S. L. Klemperer, Department of Geophysics, Stanford University, 397 Panama Mall, Mitchell Bldg. 360, Stanford, CA 94305, USA. (mkarplus@stanford.edu)

J. Mechie, Geophysical Deep Sounding Section, Deutsches GeoForschungsZentrum, Telegrafenberg E-328, D-14473 Potsdam, Germany.

D. Shi, Z. Wu, and W. Zhao, Chinese Academy of Geological Sciences, 26 Baiwanzhuang Rd., Beijing 100037, China.